ORIGINAL ARTICLE

Hydraulic fracture propagation and interaction with natural fractures by coupled hydro-mechanical modeling

Yu Hu · Quan Gan · Andrew Hurst · Derek Elsworth

Abstract Understanding the propagation of hydraulic fractures (HF) and their interaction with pre-existing fractures is essential in conducting effective stimulation in naturally fractured reservoirs. We explore fracture propagation within an equivalent continuum represented by linear elastic fracture mechanics, while updating the equivalent composite modulus of fracture and matrix based on deformation. The incremental length of fracture propagation is quantified based on the energy release rate at the fracture tips. Potential scenarios of interaction with natural fractures (crossing, arrested, or reinitiating) are interpreted through non-linear stress correction constitutive models using continuum simulator TOUGH-REACT coupled with FLAC3D. Comparison between simulations and experimental observations highlight the three principal factors controlling hydraulic fracture interaction in defining whether HFs either directly cross, are arrested by, or reinitiate from the natural fractures. Simulation results reveal that a larger approaching angle and elevated deviatoric stress both favor direct crossing due to the comingled normal stress effects on the natural fractures. Conversely, when the approach angle and deviatoric stress difference are smaller, the natural fractures hinder HF crossing and either promote arrest of the HF or enable remote reinitiation from the initial intersection where a reinitiation criterion is satisfied. Direct crossing is favored only for a threshold minimum friction coefficient representing the case where the fracture is strong, replicates intact rock strength and is mechanically "invisible". The development and verification of the model indicate the applicability in predicting the evolution of hydro-mechanical properties and fracture patterns due to the perturbation introduced by fluid pressurization. Simulation results from modelling of Panoche sand injectites reveals that the development of hydraulic fractures cause significant drawdown of borehole pressure through dissipation. Permeability evolution of fractures is concurrently evaluated based on the stress state and updated fracture geometry through dual-way coupling. The hydraulic fracture can connect natural discontinuities in sand injectites to facilitate fluid flow in otherwise low-permeability matrix, with field-scale permeability of sand injectites can be significantly increased by ~ 2 orders of

Y. Hu · Q. Gan (✉)
College of Resources and Safety Engineering, Chongqing University, Chongqing, China
e-mail: quan.gan@cqu.edu.cn

Y. Hu
CNOOC Research Institute, Beijing, China

Q. Gan · A. Hurst
Department of Geology and Geophysics, School of Geosciences, University of Aberdeen, Aberdeen, UK

D. Elsworth
Department of Energy and Mineral Engineering, EMS Energy Institute and G3 Center, Pennsylvania State University, University Park, PA, USA

🙲 Springer

magnitude. The arrest of hydraulic fracture by a natural fracture leads to fluid pressure buildup, which yields higher permeability enhancement than direct crossing of the hydraulic fracture which dissipates more pressure. Thereby, an optimized strategy for selection of well locations and injection schedules is critical in determining pattern of complex fracture networks which is beneficial in improving reservoir conductivity.

Article Highlights

- HF propagation and interaction with NFs were developed and studied in a coupled continuum simulator.
- HF may directly cross, be arrested by, or reinitiate from interacted NFs, influenced by multiple physical factors.
- Development of fracture networks in sand injectites can enhance field-scale permeability by ~ 2 orders of magnitude.

Keywords Hydro-mechanical coupling · Sand injectites · Hydraulic fracture propagation · Fracture interaction · Natural fractures · Fractured rock

1 Fracture propagation and interaction with natural fractures

Hydraulic fracture (HF) propagation in naturally-fractured tight reservoirs is a prerequisite in effectively recovering hydrocarbons by reducing the effective drainage path length from the matrix blocks. However, HFs follow a path that minimizes the expended energy in propagation (work equivalent to the product fracture-normal stress and the dilation) in exceeding the tensile strength, opening and propagating (Hubbert and Willis 1957; Valko and Economides 1995; Sarmadivale and Rasouli 2014). Thus, in the absence of other confounding influences, HFs will propagate perpendicular to the orientation of the present day minimum in-situ principal stress—with this frequently inconsistent with the previous orientation of in-situ tectonic stress that controlled the development of the relic natural fractures—both in tension and shear. Hence, hydraulic fractures and natural fractures may intersect and form complex fracture networks, which may further promote fluid

flow within the reservoir and enhance reservoir production. Therefore, it is essential to understand mechanisms controlling fracture propagation and interaction in naturally fractured reservoirs. This may be completed analytically, experimentally or numerically, to explore the influences of hydro-mechanical interactions due to the presence of natural fractures, applied stress state, rock properties and other relevant features.

A hydraulic fracture initiates and propagates when fluid over-pressure exceeds the combined impediments of in situ stress and strength (Valko and Economides 1995). Several criteria describe fracture propagation, representing a critical stress or energy state required for the fracture to grow (Lawn 1993). Linear elastic fracture mechanics may be used to represent energy-balance (Griffith 1921) and define stress concentrations (Neuber 1937) that are proportional to fracture propagation length. Nonlinear tip effects modulate propagation through plasticity and microcracking (Irwin 1948; Orowan 1949) including concepts of a cohesive zone at the tip (Barenblatt 1962; Dugdale 1960) and blunting the fracture tip singularity (Chen et al. 2009; Dugdale 1960; Barenblatt 1962; Ren et al. 2019). Energy release rates (Irwin 1956) scale with the square-root of fracture length (Renshaw and Pollard 1994) and allow stress intensity factors to define propagation direction (Paris and Erdogan 1963) and the activation of propagation. Consistent with many field and laboratory observations (Dyer 1983; Delaney et al. 1986; Pollard 1987; Atkinson 1984; Atkinson and Meredith 1987a, b; Segall 1984a, b; Olson 1993, Oslon et al. 2002), fracture propagation occurs at stress concentrations below the critical toughness (Segall 1984a; Senseny and Pfeifle 1984; Atkinson and Meredith 1987a, b; Olson 1993, 2003; Atkinson and Cook 1993) as a result of subcritical fracture failure (Atkinson 1984; Renshaw and Pollard 1994), driven by fatigue and corrosive processes (Oslon et al. 2002) and damage accumulation (Kachanov 1958; Valko and Economides 1994). The development of tip energy propagation criteria provides a powerful tool for linear elastic fracture mechanics applied in continuum modelling (Crofton 2014). Also, some analytical and experimental fracture interaction models (Blanton 1982, 1986; Warpinski and Teufel 1987) suggest higher differential stress and higher approach angles favor crossing. Criteria describe the crossing criterion

for fracture-normal approach for unbounded frictional interfaces in brittle linear elastic materials (Renshaw and Pollard 1995), numerically extended for non-orthogonal approach angles (Gu and Weng 2010). None of these crossing criteria are analytically applicable for natural fractures with cohesion and non-orthogonal approach angles. A further expansion of the Renshaw and Pollard (1995) crossing criterion has been verified for general non-orthogonal cohesive natural interfaces (Sarmadivale and Rasouli 2014)— one of the approaches considered in this work.

In summary, fractures increase the complexity of fluid flow behavior and geomechanical response within fractured media, specifically feedbacks coupled within these processes. Equivalent continuum approaches are suitable for large-scale analyses accommodating long term flow and transport behavior—such as in hydraulic fracturing simulations. The major assumption of equivalent continuum approaches is that the macroscopic behavior of the fractured rock and their constitutive relationships can be characterized by the laws of continuum mechanics (Gan and Elsworth 2016) with fracture properties implicitly embedded in the continuum models. Continuum approaches provide unique advantages in both representing fracture propagation and interaction mechanisms in large scale rock and in delivering solutions for long term simulation with significantly increased computational efficiency. Thus, we explore mechanisms of fracture propagation and interaction with nature fractures in sand injectite systems in this work, by developing fracture propagation and interaction modules in the continuum simulator platform TOUGHREACT-FLAC3D.

1.1 Geological significance

Sand injectite systems are increasingly recognized in outcrop and subsurface studies following their first description almost 200 years ago and recognition of their utility for hydrocarbon concentration and production (Dixon et al. 1995). They are typified by complex geometry, incorporate both unconsolidated and consolidated facies and the sand injectite features, such as sand intrusions contains commercial volumes of hydrocarbons (Hurst et al. 2005; Hurst and Cartwright 2007). Sand injectites form due to tectonically-induced basin-scale fluid overpressures which propagate fractures upward to form fracture networks.

Sands may also become fluidized and injected by hydraulic fracturing into otherwise low permeability units, forming sand dykes (Taylor 1982; Hurst et al. 2011). Usually, intrusions in sand injectites could be feasibly represented by discontinuities as natural fractures in the model defined by different apertures and lengths (Gan et al. 2020). These discontinuity networks can breach seals and allow fluids to communicate between reservoirs, even though sometimes separated by low permeability units spanning hundreds of meters (Huuse et al. 2005; Hurst et al. 2003; Cartwright et al. 2007; Hurst and Cartwright 2007). In sand injectites, fractures with a lower dip are typically initially longer with a larger aperture than fractures with a higher dip. After the sand is intruded into the seal breaching fractures, the higher dip sand intrusions are relatively poorly sorted, and more tightly packed with a lower porosity than the lower dip sand intrusions (Scott et al. 2013). By comparison, sand intrusions with a shallower dip are usually only moderately sorted and loosely packed with a moderate porosity. Hence, these characteristics could result in lower permeability and porosity for higher dip intruded fractures than those with shallow dip.

Basin-scale sand injectites can significantly change fluid migration paths as discontinuity distributions are significantly modified. The evolving hydraulic fracture networks within the sand injectites typically enable regional-scale inter-reservoir communication (Vigorito and Hurst 2010). However, those positive effects may be offset by deleterious impacts of early water breakthrough (Briedis et al. 2007). Therefore, it is important to understand the key features and controls of fracture propagation and interaction that form complex fracture networks and influence the fluid flow and recovery within the reservoir.

2 Methodology

We consider an elastic and low permeability reservoir with equivalent scalar and tensorial physical properties and constitutive relationships conditioned by the structural elements. The continuum simulator TOUGHREACT-FLAC3D couples the analysis of mass and energy transport in the fractured medium via TOUGHREACT (Xu et al. 2012) with mechanical deformation represented in FLAC3D (Itasca 2000). The two programs are linked by extra linking

constitutive models developed in FORTRAN (Taron and Elsworth 2009) including stress-dependent aperture and permeability evolution, composite modulus of the fractured medium, and fracture propagation and interaction mechanisms. These integrated constitutive relationships provides a tractable solution to predict the potential evolution of fracture network patterns and fluid flow in fractured rocks.

The analysis of hydraulic fracture propagation requires additional parameters including stress intensity factor and energy release rate, to quantify the strain energy near the fracture tips and to determine propagation. The magnitude of the stress intensity factor is estimated based on fracture geometry and opening stress. The energy release rate (Griffith 1921), defined as the change in elastic strain energy per unit area of fracture growth, is related to the stress intensity factor. Based on the principle of Griffith energy balance, the mechanical potential energy released during an increment of fracture growth must be no less than the potential surface energy of the newly created fracture increment (Atkinson 1987; Pollard 1987). Fractures tend to propagate along the orientation which consumes the least energy—evaluated as the product fracture-normal stress and fracture opening displacement (Li et al. 2018). A typical approach assumes that hydraulic fractures would be in the opening mode in response to the driving stress conditions (Olson 2003; Zhou et al. 2008). While the opening mode (I) consumes less energy than the other shear modes (II or III). Thus, hydraulic fractures tend to propagate along the orientation that minimizes the shear loading, following the direction perpendicular to the minimum principal stress for brittle fracturing.

When a hydraulic fracture approaches and intersects with natural fractures, the potential outcomes include: crossing, arresting at the fracture or by temporarily arresting but reinitiating from a new location on the natural fracture. Thus, fracture interactions add significant complexity in understanding the evolving structure of fractured reservoirs. Parameters such as mechanical properties, frictional angle of natural fractures and approach angle are accommodated in fracture interaction solutions based on the modified Renshaw and Pollard (1995) criterion (Sarmadivaleh and Rasouli 2014).

2.1 Fracture propagation criterion

Simulation of fracture propagation requires consideration of the evolution of fracture stress states and patterns, including fracture failure state, fracture opening stress, and orientation of fracture propagation. Fracture tip energy, quantified by the stress intensity factor, is compared with the corrosion limit of the rock matrix, to estimate failure potential at the fracture tips to propagate.

The subcritical fracture failure criterion (Olson 2003; Paluszny and Matthai 2009) is adopted, which is different from the typical fracture failure criterion. In typical fracture failure criteria, a fracture has the potential to propagate when the energy near the fracture tip exceeds the fracture toughness of the material. In comparison, the subcritical fracture failure criterion assumes that fatigue and corrosive processes near the fracture tips have progressively weakened the material near the tips. Subcritical fracture growth mechanisms, which are often found under many geologic conditions, may become the dominant mechanism for fracture propagation in long term loading environment. The long term loading environment is common in Earth's crust which can weaken a rock's fracturing strength (Anderson and Grew 1977; Atkinson 1984; Renshaw and Pollard 1994). Therefore, although the energy near the fracture tips may not overcome fracture toughness of the material, fracture propagation may still be triggered when only the material corrosion limit is exceeded, which is much smaller than the fracture toughness of the material.

The quantification of the energy at the fracture tip and the tendency for an opening fracture to propagate are assessed from the opening-mode stress intensity factor K_I (Lawn and Wilshaw 1975). The opening-mode stress intensity factor K_I is approximated as (Lawn and Wilshaw 1975),

$$K_I = \sigma_0^I \sqrt{\pi a} \tag{1}$$

where σ_0^I is the fracture opening stress and a is the hydraulic fracture half length.

However, the stress field ahead of the fracture tip can be significant even with the singular characteristics during of fracture propagation. This implies that a yielded region will exist in the rock material ahead of the fracture tip. Thus, a non-linear stress correction near the fracture tips is necessary to improve the

accuracy of the stress response triggered by local plastic deformation. Continuous loading could result in the development of many microcracks forming near the tip, inducing non-linear mechanical behavior ahead of the fracture tip with the diffusion of the stress concentration. Macrocrack extension will occur due to the linking of those microcracks in this non-linear yielded fracture-process zone (Atkinson 1987). The existence of a yielded zone matches with experimental observations (Ghamgosar and Erarslan 2016), which is associated with energy dissipation due to fracture growth (Evans and Charles 1976; Hillerborg et al. 1976). Averaging behavior of those many microcracks in the fracture process zone around the main fracture tip simplifies the complex problem of tip propagation. Thus, it is appropriate to represent the average behavior by using a single macrofracture within the process zone (Costin 1987).

A subcritical fracture propagation criterion which is material dependent is applied within the weakened and non-linear fracture process zone, where the fracture tip fails and starts to propagate. Thus, a lower threshold of stress intensity factor (K_{IC}^*) is needed to evaluate fracture propagation, compared to the intrinsic fracture toughness of the intact material (K_{IC}) (Atkinson 1984),

$$K_{IC}^* \leq K_I \leq K_{IC} \tag{2}$$

where it is assumed that $K_{IC}^* = 0.1K_{IC}$ considering subcritical crack growth can be present at very low stress intensities (from $0.05K_{IC}$ to $0.4K_{IC}$) (Karunaratne and Lewis 1980; Evans and Blumenthal 1983; Segall 1984a; Atkinson and Meredith 1987b; Olson 1993).

2.2 Effective fracture length, stress intensity factor update, and stress correction

Based on the theory of subcritical crack propagation, two zones are considered to describe the stress field near the fracture tip (Fig. 1). The inner zone adjacent to the fracture tip defines the non-linear fracture process zone in which stress intensity factor is adjusted due to the yielding process. The outer zone is the K-field (near-tip elastic stress field) (Sun and Jin 2012). Stress tensors are corrected in both zones based on the updated stress intensity factor and the near tip-field solution (Irwin 1958; Wells 2001).

Fracture size is usually large compared to the size of the fracture process zone. Idealizing the fracture process zone as circular and under plane strain conditions, allows an estimate of the radius (R_p) of fracture process zone as (Gdoutos 2003; Sun and Jin 2012)

$$R_p = \frac{1}{6\pi}\left(\frac{K_I}{\sigma_{YS}}\right)^2 \tag{3}$$

where K_I is the standard stress intensity factor (Eq. (1)) and σ_{YS} is the yield strength of the rock material. This equation is valid for the plastic fracture process zone (Schmidt and Lutz 1979). Plastic deformation near the fracture provides the illusion of a slightly longer macrofracture than the actual macrofracture length ($2a$). This presumed slightly longer macrofracture is defined as an effective fracture, which is longer than the actual fracture by the half length of the non-linear zone. The half-length of the effective fracture A_{eff} is defined as (Irwin 1960; Sun and Jing 2012)

$$A_{eff} = a + R_p \tag{4}$$

As Irwin's model (1960) assumes that the adjusted stress intensity factor for fracture propagation in fracture process zone still follows linear elastic fracture mechanics criterion in the presence of small-scale plastic deformation, stress intensity factor K_I' is adjusted due to fracture tip plasticity by using the half length of the effective fracture as (Irwin 1960; Sun and Jin 2012)

$$K_I' = \sigma_0^I\sqrt{\pi A_{eff}} \tag{5}$$

It is assumed that stress decays exponentially away from the fracture tip following the rule of near-field solutions in the K-field (Irwin 1958; Paluszny and Matthai 2009). Based on this assumption, multiple transient elements near the fracture tip element are regarded as the components of the K-field for the near-tip stress correction (Fig. 2). These transient elements have different and transient distances from the fracture tip, provided to increase the accuracy and decrease in the jump in values in the transient elements in the near-tip stress calculations. This response indicates that the influence of the local stress concentration of the tip is not limited to the fracture tip element but extends to some distance away from the fracture tip.
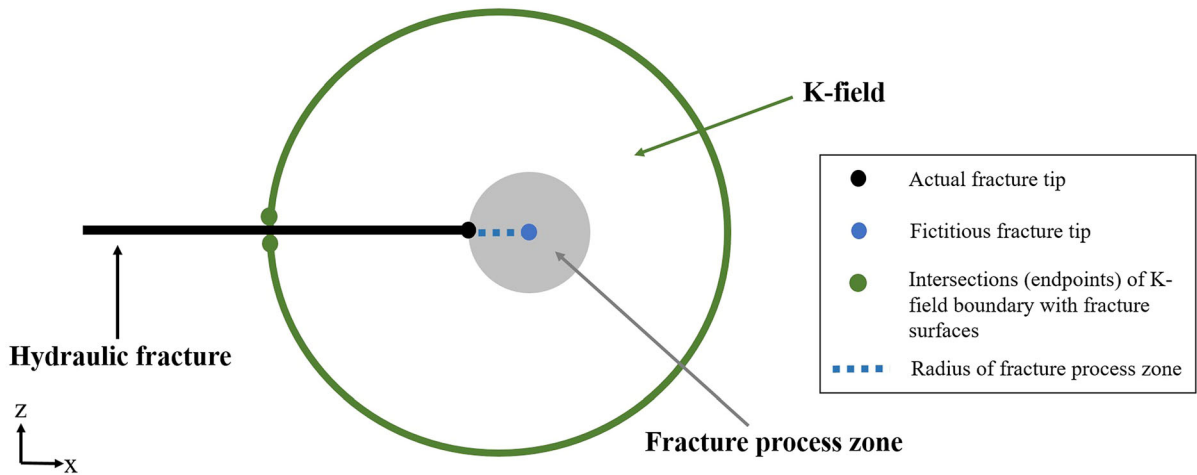
Fig. 1 Schematic drawing of fracture process zone and K-field near a hydraulic fracture tip (revised from Atkinson 1987; Sun and Jin 2012)
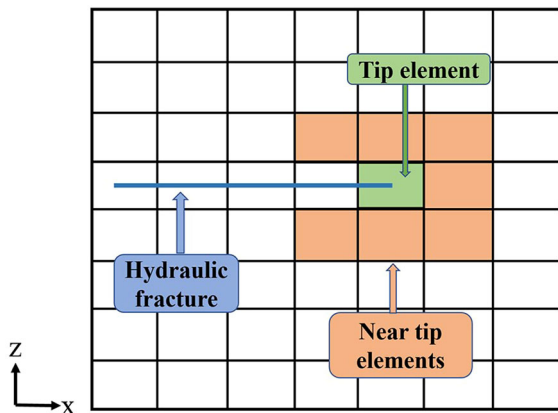

Fig. 2 Schematic of near tip elements (orange) near the element of the hydraulic fracture tip (green) for K-field (near-tip stress field) calculations

Combining the effects of the fracture process zone with the near-tip solutions, the stress tensor correction that defines the stress field in the K-field under mode I loading conditions is expressed as,

$$\sigma_x = \frac{K_I'}{\sqrt{2\pi r}} \cos\frac{\theta}{2}\left(1 - \sin\frac{\theta}{2}\sin\frac{3\theta}{2}\right) \tag{6}$$

$$\sigma_z = \frac{K_I'}{\sqrt{2\pi r}} \cos\frac{\theta}{2}\left(1 + \sin\frac{\theta}{2}\sin\frac{3\theta}{2}\right) \tag{7}$$

$$\sigma_y = \upsilon(\sigma_x + \sigma_z) \tag{8}$$

$$\tau_{xz} = \frac{K_I'}{\sqrt{2\pi r}} \cos\frac{\theta}{2}\sin\frac{\theta}{2}\cos\frac{3\theta}{2} \tag{9}$$

where σ_x, σ_z and σ_y are the near-tip normal stresses parallel and perpendicular to the fracture plane and vertical to the x–z loading plane, respectively. τ_{xz} is the near-tip shear stress on the same fracture plane. r is the radial distance from the fracture tip, K_I' is the adjusted opening-mode stress intensity factor, υ is the Poisson ratio and $\theta(0 \leq \theta < \pi)$ is the counter-clock-wise angle rotated from the original orientation of the fracture plane. The fracture surfaces behind the fracture tip ($\theta = \pi$) are open.

Because stresses at the fracture tip are singular, the non-local tip stress tensors are derived as a weighted average of the stresses within an interaction radius near the tip (Mergheim et al. 2005). A Gaussian weighting function (Eq. (10)) is applied to the stress tensors of the adjacent transient elements near the tip to derive the tip stress tensors at the Gauss points (integration points). This Gaussian weighting function is defined as (Wells 2001),

$$w(r) = \frac{\hat{w}(r)}{\sum_{i=1}^{n_{gp}} \hat{w}_i A_i}, \; \hat{w}(r) = \frac{1}{l\sqrt{2\pi}}\exp\left(\frac{-r^2}{(2l)^2}\right), \tag{10}$$

where r is the distance from the fracture tip to the integration points of the neighboring transient elements; l is a coefficient that determines how quickly the weighting function decays away from the fracture tip and is taken as approximately three times the element dimension (Wells 2001).

Based on the weighting factor (Eq. (10)), a non-local stress tensor $\hat{\sigma}(\boldsymbol{x})$ which represents the stress tensor integrated at the tip element is obtained from the sum of the stress tensors at the Gauss points i weighted with the weighting factor w_i and the associated area A_i as,

$$\hat{\sigma}(\boldsymbol{x}) = \sum_{i=1}^{n_{gp}} \boldsymbol{\sigma_i} w_i A_i \tag{11}$$

where n_{gp} is the number of the adjacent elements near the fracture tip included in the near-tip elastic stress field and $\boldsymbol{\sigma_i}$ is the stress tensor in the adjacent element i.

2.3 Fracture propagation incremental length

Gurney and Hunt (1967) demonstrated that for dynamic fracture growth, the energy required to propagate a fracture is inversely proportional to the square-root of the fracture length. Fracture propagation velocity is related to the maximum incremental propagation length at any propagation step by means of a power law, e.g. a Paris-type law. This type of power law method may be used to estimate simultaneous fracture growth from multiple fracture tips (Paris and Erdogan 1963; Zi et al. 2004). A well-established propagation criterion originally defined by Charles (1958) and then extended by Renshaw and Pollard (1994) is implemented to predict incremental propagation length. This method accommodates the energy accumulated near a fracture tip which exponentially derives fracture growth by weighing the energy with an empirical velocity index α (Olson et al. 2002). These results imply that fracture tips with higher energy grow faster than fracture tips with lower energy. The incremental fracture propagation length (l_{adv}) ahead of a fracture tip is estimated as (Renshaw and Pollard 1994; Paluszny and Matthai 2009),

$$l_{adv} = l_{\max} \left(\frac{G}{G_{max}} \right)^{\alpha}, \ G = \frac{(K_I^{'})^2 (1 - v^2)}{E} \tag{12}$$

where $l_{\max}$ is the maximum incremental length per propagation step assigned as the initial fracture size (Paluszny and Matthai 2009); G is the energy release rate under plain strain condition; $K_I^{'}$ is the updated stress intensity factor (Eq. (5)); v is the Poisson ratio and E is the Young's modulus of the matrix and G_{max} is the maximum energy release rate among all the hydraulic fracture tips at the current propagation step. From exhaustive experimentation, the index $\alpha = 0.35$ was adopted which could yield realistic fracture patterns for rock analogues (Renshaw and Pollard 1994). Moreover, since $G \leq G_{max}$, fracture propagation incremental length l_{adv} is expected not to exceed the maximum fracture propagation increment $l_{\max}$ (Paluszny and Matthai 2009; Taleghani 2009).

2.4 Fracture interaction criteria

Fracture interaction is controlled by a limited number of key parameters. These include stress states, mechanical properties of the natural fractures and rock matrix, approach angle between the hydraulic fracture and the natural fractures and friction angle of the natural fractures. Several analytical criteria such as the Blanton criterion (1982, 1986) are invalid for small approach angles, while the Renshaw and Pollard criterion (1995) only works for an orthogonal approach. In comparison, the modified Renshaw and Pollard (1995) criterion (Sarmadivaleh and Rasouli 2014) (Eq. (13)) is suitable for more general cases where the approach angle is non-orthogonal. This criterion has been developed based on the assumption that the induced fracture could propagate directly to the other side of the natural fracture (direct crossing) when the tensile stress field ahead of the hydraulic fracture tip is sufficient to be transferred to the opposite side of the natural fracture interface. The effects of far-field stresses and the near-tip stress field are considered in the criterion (Renshaw and Pollard 1994; Sarmadivaleh and Rasouli 2014). A linear elastic, homogeneous, isotropic rock mass on both sides of the natural fracture interface is assumed. When the fracture crossing criterion (Eq. (13)) is satisfied, the hydraulic fracture is expected to directly cross the natural fractures and continue propagating on the opposite side (Fig. 3a). The criterion is,
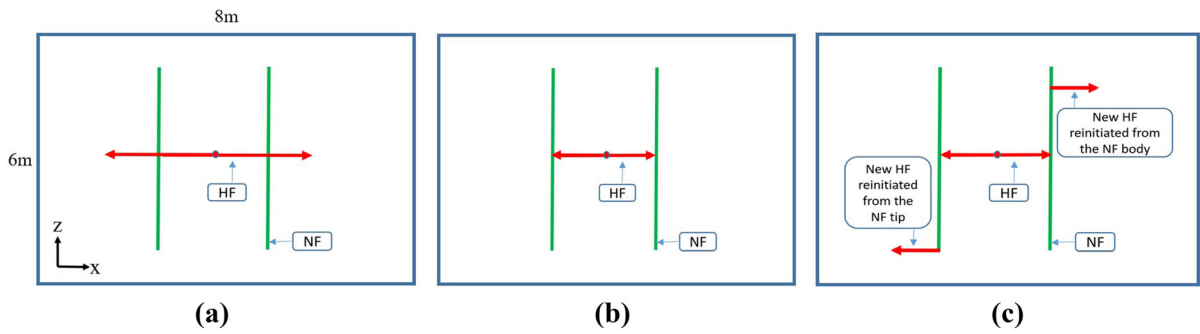
Fig. 3 Scenario schematic of (**a**) direct crossing; (**b**) staying arrested; (**c**) reinitiating. The green lines represent natural fractures. The red lines represent hydraulic fractures in which the arrows stand for propagation directions. The circle in the model center symbolizes the injection well

$$\frac{-\sigma_n}{T_0 - \sigma_T} > \frac{\left(1 - \sin\frac{\theta}{2}\sin\frac{3\theta}{2}\right) + \frac{1}{\mu_f'' \cos\frac{\theta}{2}}\left|\sin\frac{\theta}{2}\cos\frac{\theta}{2}\cos\frac{3\theta}{2} + \alpha\right|}{1 + \sin\frac{\theta}{2}\sin\frac{3\theta}{2}}$$

(13)

where θ is the approach angle, T_0 is the rock tensile strength, σ_n is the normal stress and σ_T is the tangential stress. These normal and shear stresses are defined as

$$\sigma_n = \frac{\sigma_{HMax} + \sigma_{hMin}}{2} + \frac{\sigma_{HMax} - \sigma_{hMin}}{2}\cos(\pi - 2\theta)$$

(14)

$$\sigma_T = \frac{\sigma_{HMax} + \sigma_{hMin}}{2} - \frac{\sigma_{HMax} - \sigma_{hMin}}{2}\cos(\pi - 2\theta)$$

(15)

in which σ_{HMax} and σ_{hMin} are the maximum and minimum principal stresses, respectively (Eqs. (14), (15) and (17)). From these, the shear stress τ along the interface of the natural fracture (Jaeger et al. 2007) and the shear stress coefficient α related to near-tip shear stress (Eq. (16)) are defined as

$$\alpha = \frac{\tau}{\frac{T_0 - \sigma_T}{\cos\frac{\theta}{2}\left(1 + \sin\frac{\theta}{2}\sin\frac{3\theta}{2}\right)}}$$

(16)

$$\tau = -\frac{\sigma_{HMax} - \sigma_{hMin}}{2}\sin(\pi - 2\theta)$$

(17)

and $\mu_f'' = \mu_f + \mu_f'$ in which μ_f is the coefficient of friction of the natural fracture, and μ_f' is,

$$\mu_f' = \frac{\frac{\tau_0}{\sigma_n}}{\frac{1 - \sin\frac{\theta}{2}\sin\frac{3\theta}{2}}{\left(1 - \sin\frac{\theta}{2}\sin\frac{3\theta}{2}\right) + \frac{1}{\mu_f \cos\frac{\theta}{2}}\left|\sin\frac{\theta}{2}\cos\frac{\theta}{2}\cos\frac{3\theta}{2} + \alpha\right|} - 1}$$

(18)

Conversely, if the criterion in Eq. (13) is not satisfied, the hydraulic fracture will be either arrested by (Fig. 3b) or reinitiate from (Fig. 3c) the natural fracture, instead of directly crossing the natural fracture. When a hydraulic fracture approaches the natural fracture, the perturbed stress field ahead of the propagating fracture tip results in aperture enhancement around the point of intersection. When the hydraulic fracture propagates into the intersection point, the magnitude of opening and the driving stress at the hydraulic fracture tip is reduced by the increasing volume of fluid entering the natural fracture. In this circumstance, the hydraulic fracture will first arrest at the natural fracture, at least momentarily and with further pressurization may transit along the natural fracture and reinitiate (Dollar and Steif 1989). This pressurization at the intersection also increases the fluid pressure inside the natural fracture, with the potential of shear failure or opening.

When the fluid pressure P_{fluid} of the natural fracture exceeds the reinitiation resistance σ_{resis} ($P_{fluid} > \sigma_{resis}$), the hydraulic fracture will meet the condition to reinitiate from the natural fracture. The newly reinitiated hydraulic fracture will propagate to the other side of the natural fracture from an assumed initial flaw length which is the same as the defined initial fracture size. Reinitiaiton may occur from (1) the extremity of the tips of the natural fracture; or (2) any location between the tips on the natural fracture. We examine these conditions separately:

The condition of reinitiation from the natural fracture is satisfied when,

$$\sigma_{resis} = P_{fluid} - \sigma_{reinitiation\_strength} > 0$$

(19)

where σ_{resis} is the reinitiation resistance along the natural fracture; P_{fluid} is the fluid pressure of the natural fracture and is positive; $\sigma_{reinitiation\_strength}$ is the reinitiation strength which defines the likelihood of reinitiation from the natural fracture. Thus conditions for reinitiation may be defined as:

(1) Reinitiate from natural fracture tips.

$$P_{fluid} > \sigma_{reinitiation\_strength} = |\sigma_3| + T_0 \qquad (20)$$

where σ_3 is the local minimum principal stress at potential reinitiation tips on natural fractures considering the strong influence of the natural fracture on local stress; T_0 is the tensile strength of the rock which is assumed null as the natural fracture tips are assumed to have failed in tension and opened (Sarmadivaleh and Rasouli 2014).

(2) Reinitiate from natural fracture bodies.

$$P_{fluid} > \sigma_{reinitiation\_strength} = \max(|\sigma_3| + T_0, |\sigma_{norm}|) \qquad (21)$$

$$\sigma_{norm} = \frac{\sigma_{max} + \sigma_{min}}{2} + \frac{\sigma_{max} - \sigma_{min}}{2}\cos(\pi - 2\theta) - \tau\sin(\pi - 2\theta) \qquad (22)$$

where σ_{norm} (Eq. (22)) is the local total normal stress which examines whether the targeted location on the natural fracture body opens or not (Jaeger 1979); the *max* operator in Eq. (21) takes the maximum value of the terms in the brackets. To reinitiate from the natural fracture intermediate between the tips, the reinitiation location on the natural fracture is assumed to open and its reinitiation resistance is overcome by fluid pressure within the natural fracture. σ_1, σ_3 and τ are the maximum principal stress, minimum principal stress, and shear stress at the potential reinitiation location on the natural fracture, respectively, and θ is the approach angle (Fig. 4).

3 Algorithm for fracture propagation and interaction

The workflow for the fracture propagation and intersection modelling is illustrated in Fig. 5. This cycle begins with equilibration of temperature and fluid pressure in TOUGHREACT. Subsequently, fracture pattern information, such as fracture geometries and moduli, are input into a FORTRAN executable. The composite fracture moduli and equilibrium fluid pressures are parsed into FLAC3D to perform the stress–strain simulation. Fracture propagation and interaction state are evaluated according to the current stress state. If the fracture propagation criterion is satisfied, the hydraulic fracture propagates by a defined increment of extension with the network geometry correspondingly updated. When the hydraulic fracture approaches the natural fractures, the constitutive fracture interaction criteria is evaluated

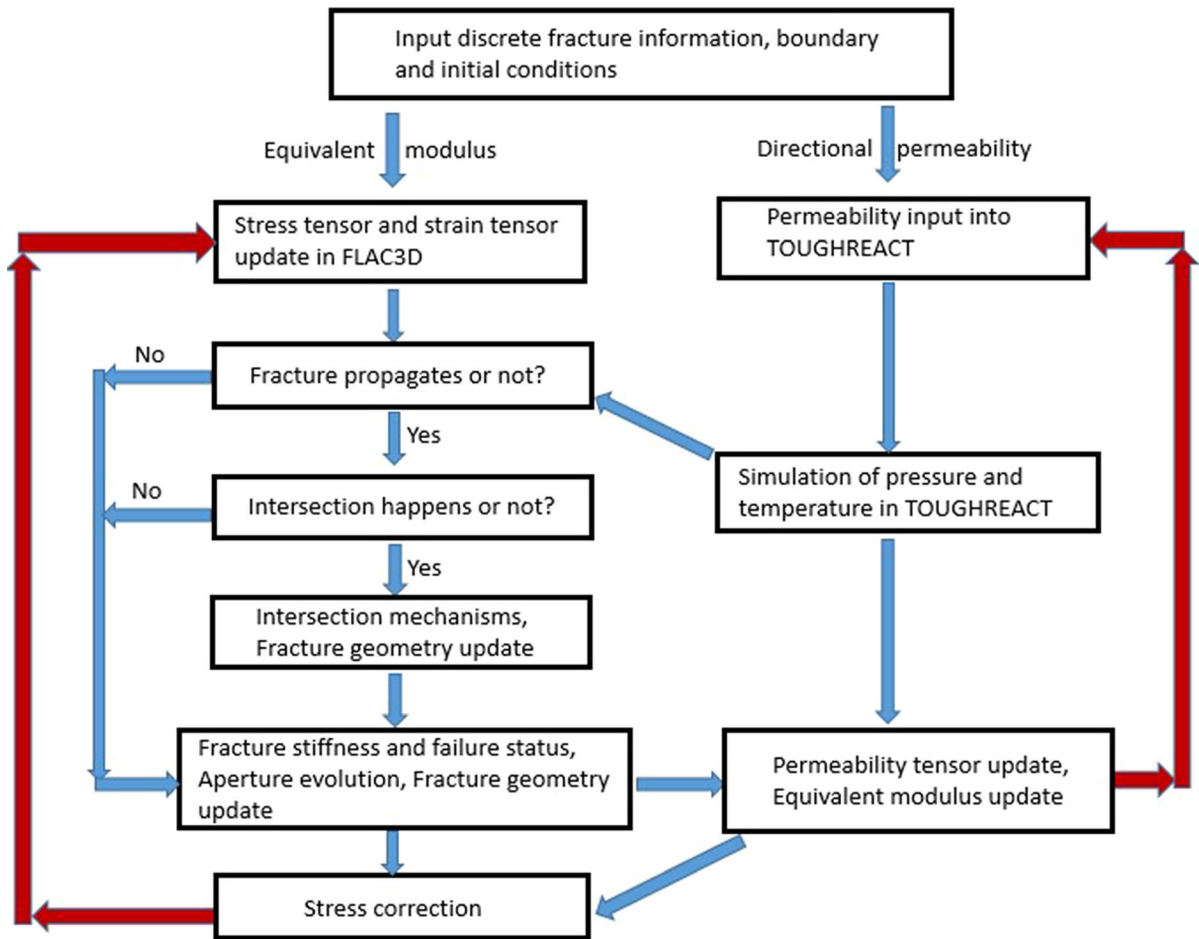Fig. 4 Distribution of reinitiation resistance along the nature fracture
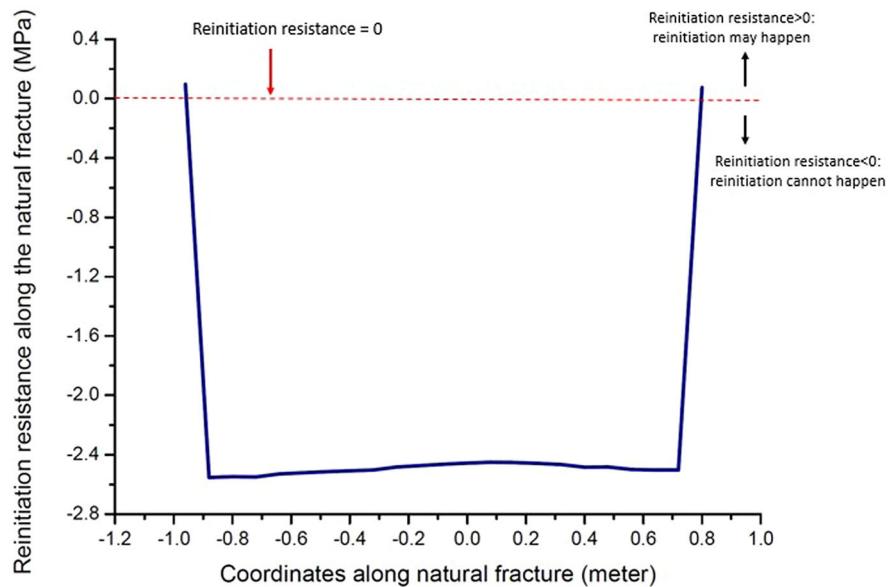
Fig. 5 Equivalent continuum simulation workflow implementation of fracture propagation in TOUGHREACT-FLAC3D.

to estimate the range of potential interaction mechanisms between the hydraulic and natural fractures. Thereafter, the stress-dependent aperture and permeability are calculated through two-way coupling in the code based on the updated fracture geometry. The induced propagation changes both fracture geometry, and associated equivalent mechanical properties, requiring the range of composite moduli of the fractured medium to be simultaneously updated. The stress field is perturbed by fracture propagation. Hence, the two-way coupling reflects the influence of both hydro-mechanical properties and the evolution of the fracture network in changing the stress field, mechanical modulus, fluid pressure, and flow paths.

4 Verification

The propagation of hydraulic fractures and their interaction with natural fractures have been investigated through field tests, laboratory experiments and numerical simulations (Blanton 1982, 1986; Renshaw and Pollard 1995; Zhang and Jeffery 2006; Zhou et al. 2008; Gu and Weng 2010; Liu et al. 2014; Sarmadi-valeh and Rasouli 2014). These results predict and define three primary types of fracture interactions: direct crossing, arrest, and deflection along the natural fracture and reinitiation from the natural fracture face or tip. The simulation results were validated and calibrated against these various configurations for single and isolated natural fractures and extend modeling to the case for the interaction of multiple fractures comprising a network.

Fig. 6 Schematic of a hydraulic fracture approaching the natural fractures. The green lines represent natural fractures. The red line represents hydraulic fracture. The circle in the model center stands for the injection well
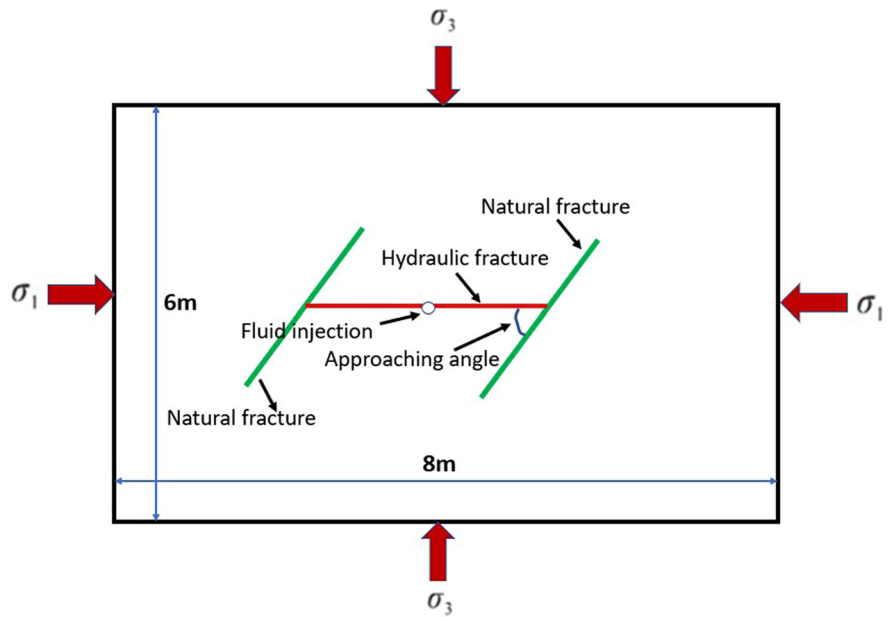
4.1 Model setting

A model representing fluid injection into a fractured reservoir was developed to verify the predictions of fracture propagation and interaction by comparing numerical simulation results against a series of experimental observations (Zhou et al. 2008; Sarmadivaleh and Rasouli 2014). The constructed model (Fig. 6) comprises a central injection well flanked by two parallel natural fractures. The model is 8 m × 6 m × 0.03 m in dimension (Zhou et al. 2017a, b) with embedded natural fractures 2 m in length. The initial aperture of the bi-wing hydraulic fracture, including the newly propagated and newly reinitiated increments, is 2.5×10^{-4} m, and the initial aperture of the natural fractures is 6×10^{-4} m (Odling 1997; Gan and Elsworth 2016). The evolution of the stress dependent aperture is captured in Eq. (23), incorporating normal closure, shear dilation, and tensile opening with permeability defined as 100 mD (Wan et al. 2015; Zhou et al. 2017a, b). Directional permeability of the hydraulic fracture is defined as k_{ij} in Eq. (24) (Gan and Elsworth 2016) which considers fracture orientation and fracture volume truncated in the fractured grid.

The maximum principal stress is in the horizontal (x-axis) direction, and the minimum principal stress is in the vertical (z-axis) direction (Fig. 6). The initial parameters are defined in Table 1 (Zhou et al.

Table 1 The initial properties of the rock mass and natural fractures that are input into the simulator (Atkinson and Cook 1993; Zhou et al. 2008; Wan et al. 2015; Gan and Elsworth 2015; Selvadurai et al. 2018)

Young's modulus (GPa)	8.4
Poisson's ratio	0.23
Initial fracture normal stiffness (GPa/m)	1300.0
Initial fracture shear stiffness (GPa/m)	500.0
Rock tensile strength (MPa)	3.73
Fracture cohesion (MPa)	0.5
Grain density (kg/m³)	2350.0
Injection rate (kg/s)	0.0002
Fracture toughness (MPa√m)	1.5
Fracture dilation angle (°)	3.0
Natural fracture friction angle (°)	20.81/41.67/50.42
Natural fracture orientation (°)	30.0/60.0/90.0

2017a, b; Sarmadivaleh and Rasouli 2014; Gan and Elsworth 2016). Limitation of LEFM in representing fracture initiation require the fracture to initiate from a very small initial flaw length of 4×10^{-3} m.

$$b = b_{ini} - \frac{9b_{ini}\sigma'_n}{\sigma_{nc} + 10\sigma'_n} + \frac{\tau - \tau_{sc}}{K_s}\tan\phi_d + \frac{(P_f - P_{f0})}{10 \times \frac{2G}{3r}}$$
(23)

where the final three terms refer to the magnitude of aperture change induced by normal closure, shear

dilation and fracture normal opening, respectively (Gan and Elsworth 2016). b is the resulting fracture aperture; b_{ini} is the initial aperture prior to the application of the principal stresses; σ'_n is the normal stress; σ_{nc} is the critical normal stress corresponding to the maximum aperture closure; K_s is the critical shear stiffness of the aperture; τ is the fracture shear stress; τ_{sc} is the critical shear stress as equivalent to the fracture shear stress when shear failure is activated; $(P_f - P_{f0})$ is the fracture pressure increase after tensile opening; G is the shear modulus of the intact rock and r is the fracture half length. The permeability tensor for the combined rock and fracture network are defined as,

$$k_{ij} = \sum^{fracnum} \frac{1}{12}(P_{kk}\xi_{ij} - P_{ij})$$
$$= \sum^{fracnum} \frac{1}{12}\left(\frac{V_{ratio}}{b_{ini}}b^3 n_k^2 \xi_{ij} - \frac{V_{ratio}}{b_{nin}}b^3 n_i n_j\right) \quad (24)$$

where b_{ini} is the initial aperture of the fracture; V_{ratio} is the fracture volume intersected in the fractured grid; $P_{i,j,k}$ is a coefficient intrinsic to the tensor (Oda 1986); ξ_{ij} is the Kronecker delta, and; $n_{i,j,k}$ is the unit normal to the fracture plane.

4.2 Verification results

We verify the numerical model against experimental observations (Zhou et al 2008, 2017a, b; Sarmadivaleh and Rasouli 2014). The heuristics first evaluate the potential for the HF to directly cross the fracture by using a modified Renshaw and Pollard criterion (Eq. (13)). If this is not met, then the hydraulic fracture will arrest and either terminate or reinitiate from elsewhere along the fracture—dependent of the environmental conditions and material properties.

Tables 2, 3 and 4 and Figs. 8, 9 and 10 document the results of the various comparisons between experimental observations (Zhou et al. 2008) and the numerical simulation results from TOUGHREACT-FLAC3D. These results are categorized into three groups according to three different frictional angles of the natural fractures (Type I: 20.81°; Type II:41.67°; Type III:50.42°) with natural fracture orientations of 30, 60, and 90 degrees considered for each of the three (I, II, III) frictional angles (Fig. 7).

In Tables 2, 3 and 4 and Figs. 8, 9 and 10, the laboratory experimental results and the numerical simulation results show a reasonably good agreement except for a few cases, which are marked in bold. Several inconsistent comparisons for low and intermediate friction (Type I and II) crossings may result from the complex heterogeneous local tensile strength of the rock, and the limited data defining local stresses, rock properties and fracture treatment during the experimental tests. The inconsistent comparison for high friction crossings (Type III) could be a result of the especially thickened material used to represent the coefficient of friction in the Type III artificial natural fractures in the experiments. The thickened material alters the mechanical properties of the artificial natural fractures and the nearby rock in the experiments (Zhou et al. 2017a, b). Given the reasonable matches between the numerical and experiment observations in the majority of the cases, we apply the continuum simulator TOUGHREACT-FLAC3D to numerically investigate the behaviors of fracture propagation and interaction through parametric analyses—to probe response for simple fracture systems with fracture

Table 2 Type I internal friction angles of the natural fractures (20.81°)

Approaching angle (deg)	σ_{max}(MPa)	σ_{min}(MPa)	Experimental results	Numerical results	Figure 8
90	8	3	Direct crossing	Direct crossing	I-1
90	8	5	**Direct crossing**	**Arrested**	I-2
60	10	3	**Direct crossing**	**Reinitiating**	I-3
60	8	3	No direct crossing	Reinitiating	I-4
30	10	3	No direct crossing	Reinitiating	I-5
30	8	3	No direct crossing	Reinitiating	I-6

Table 3 Type II internal friction angles of the natural fractures (41.67°)

Approaching angle (deg)	σ_{max} (MPa)	σ_{min} (MPa)	Experimental results	Numerical results	Figure 9
90	10	5	Direct crossing	Direct crossing	II-1
90	10	3	Direct crossing	Direct crossing	II-2
60	10	3	Direct crossing	Direct crossing	II-3
60	13	3	Direct crossing	Direct crossing	II-4
60	8	5	**No direct crossing**	**Direct crossing**	II-5
30	10	5	No direct crossing	No direct crossing: staying arrested	II-6
30	8	5	No direct crossing	No direct crossing: staying arrested	II-7
30	13	3	No direct crossing	No direct crossing: reinitiating	II-8

Table 4 Type III internal friction angles of the natural fractures (50.42°)

| Approaching angle (deg)	σ_{max} (MPa)	σ_{min} (MPa)	Experimental results	Numerical results	Figure 10
90	8	3	**No direct crossing**	**Direct crossing**	III-1
90	13	3	Direct crossing	Direct crossing	III-2
60	13	3	**No direct crossing**	**Direct crossing**	III-3
60	10	3	**No direct crossing**	**Direct crossing**	III-4
30	13	3	No direct crossing	No direct crossing: reinitiating	III-5
30	8	3	No direct crossing	No direct crossing: reinitiating	III-6
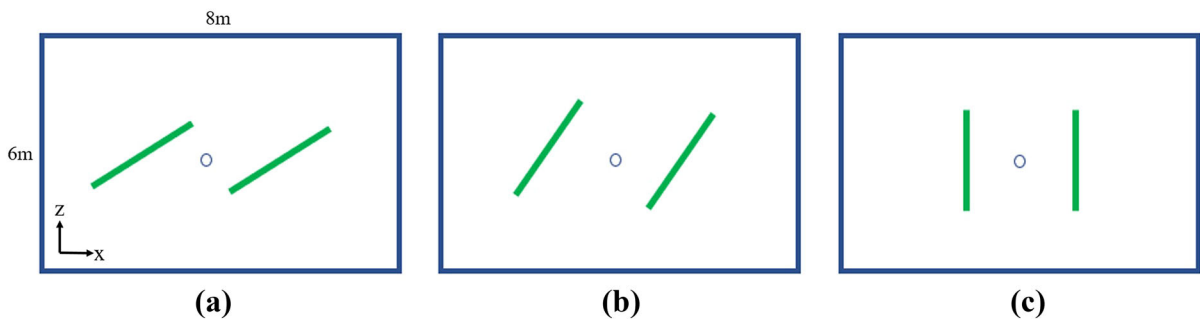
Fig. 7 Scenarios of different natural fracture orientations. (**a**) 30 degrees. (**b**) 60 degrees. (**c**) 90 degrees. The green lines represent the natural fractures. The white circle represents the injection well

interaction among multiple natural fractures examined in a subsequent companion paper (Figs. 11, 12).

Furthermore, the influence of different approach angles, stress differences, and friction angles of the natural fractures can be analyzed according to these simulation results. Comparison among simulation cases I-1, I-4 and I-6 (constant low friction and increasing approach angle) reveal that higher approach angles apply progressively higher

compressive stresses to the natural fracture. This results in greater normal closure on the natural fracture and therefore an increased propagation pressure available for the transfer of tensile stress across the natural fracture (via friction), favoring direct crossing. In comparison, lower approach angles favor arrest at the intersection point until the onset of reinitiaiton from weaker points on the natural fracture can be mobilized. Comparison between cases for low friction
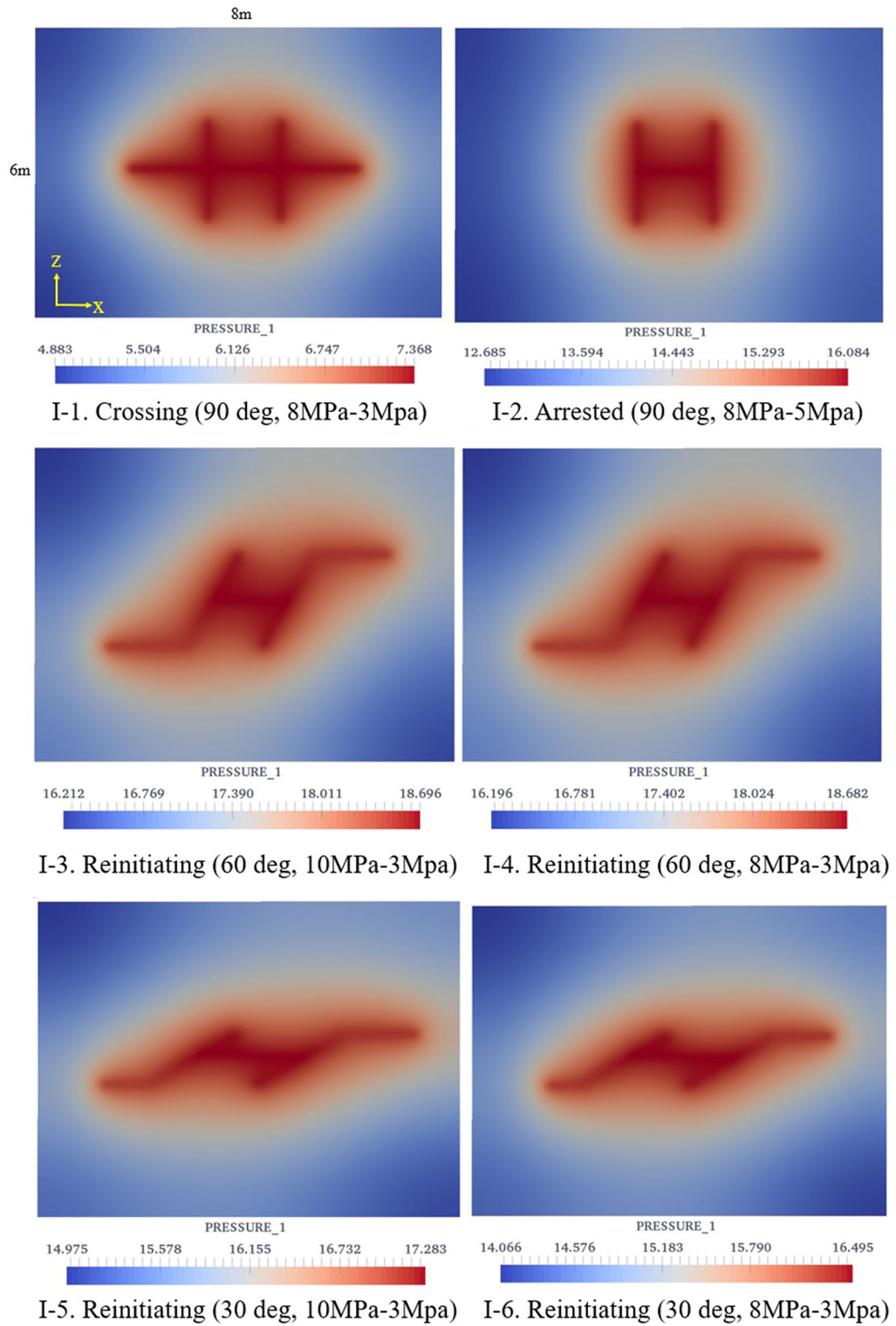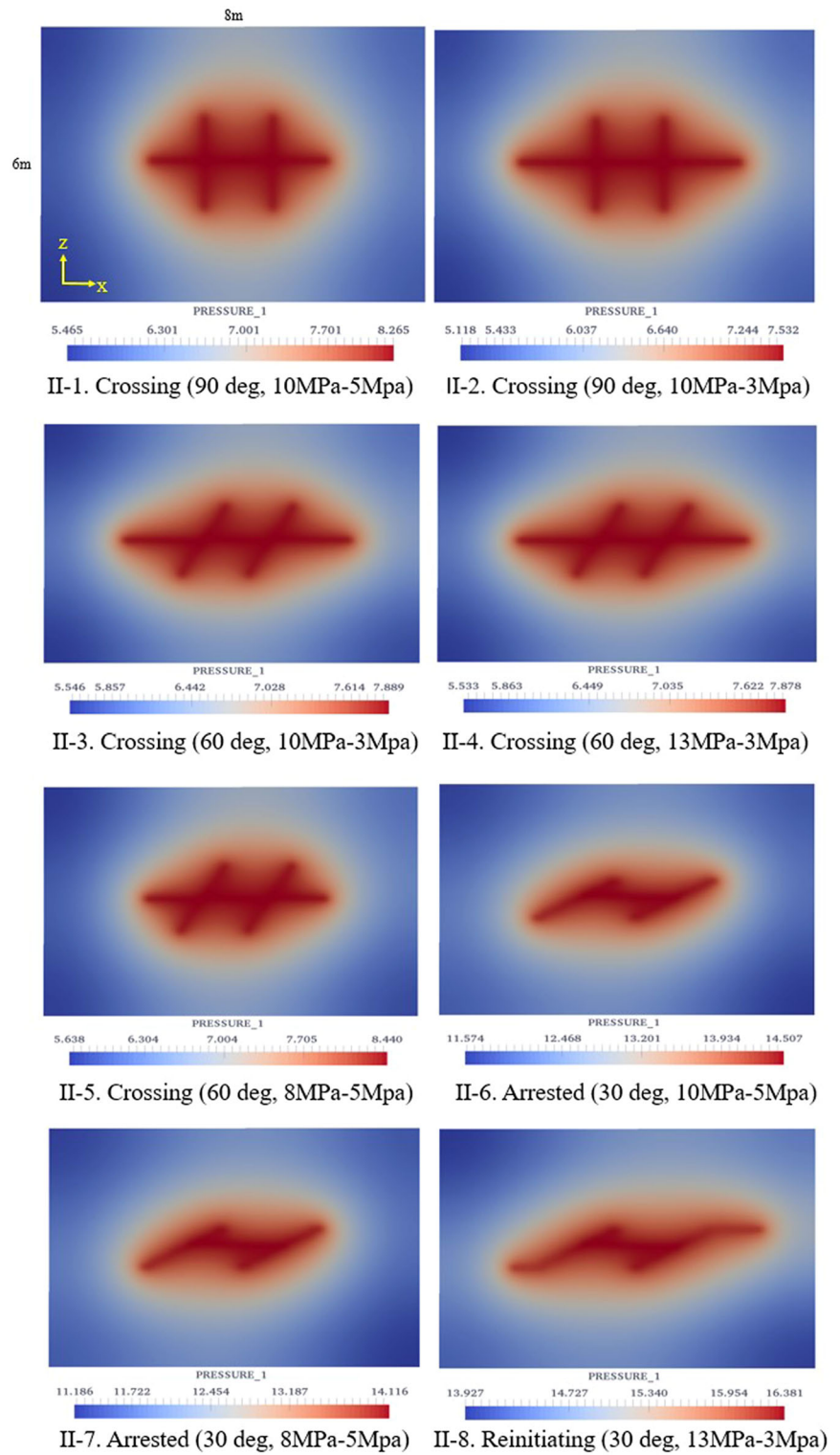
Fig. 8 Simulation results of Type I internal friction angles of the natural fractures (20.81°)

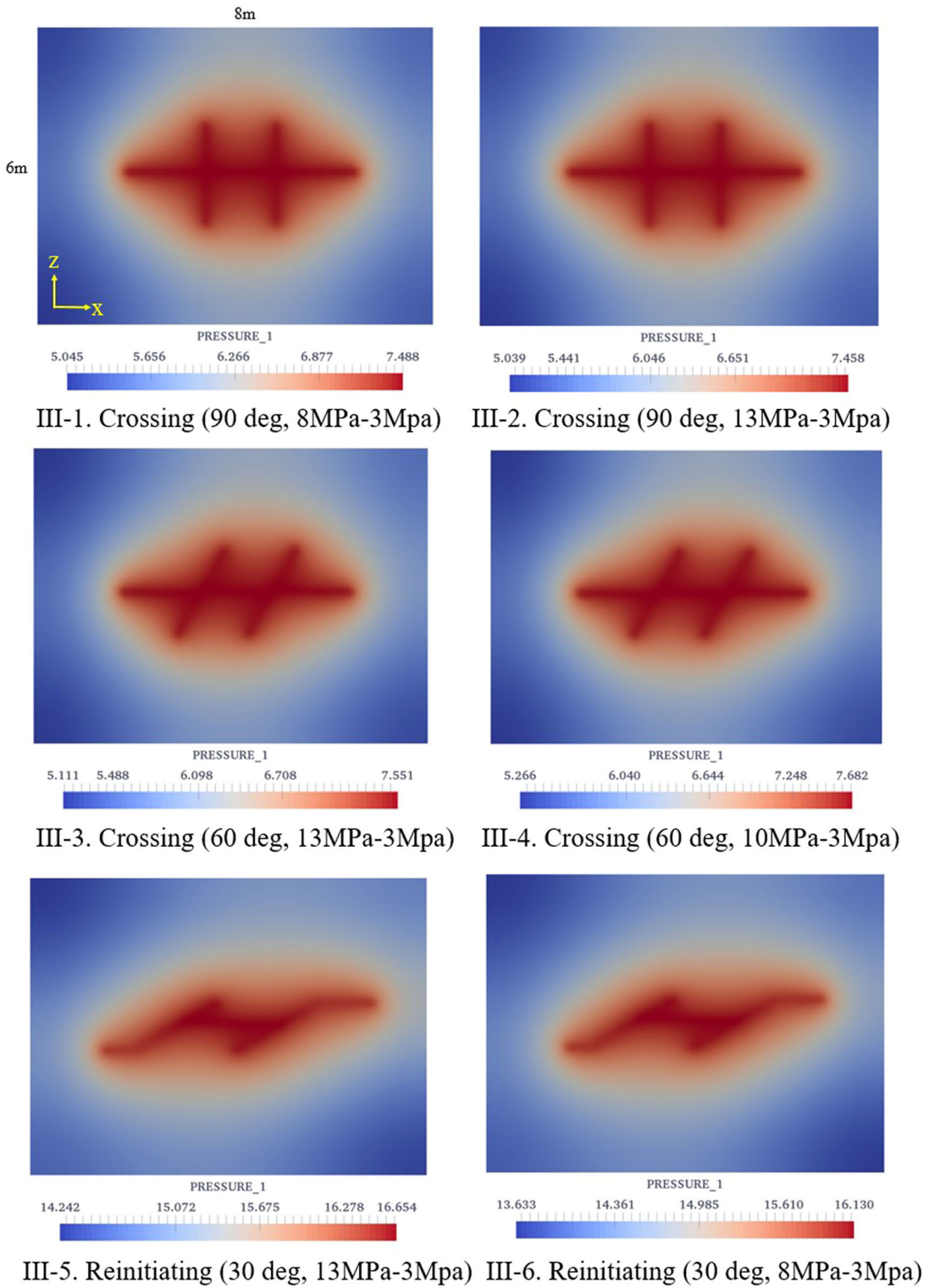**Fig. 9** Simulation results of Type II internal friction angles of the natural fractures (41.67°)

8m

6m

II-1. Crossing (90 deg, 10MPa-5Mpa)

II-2. Crossing (90 deg, 10MPa-3Mpa)

II-3. Crossing (60 deg, 10MPa-3Mpa)

II-4. Crossing (60 deg, 13MPa-3Mpa)

II-5. Crossing (60 deg, 8MPa-5Mpa)

II-6. Arrested (30 deg, 10MPa-5Mpa)

II-7. Arrested (30 deg, 8MPa-5Mpa)

II-8. Reinitiating (30 deg, 13MPa-3Mpa)

Fig. 10 Simulation results of Type III internal friction angles of the natural fractures (50.42°)
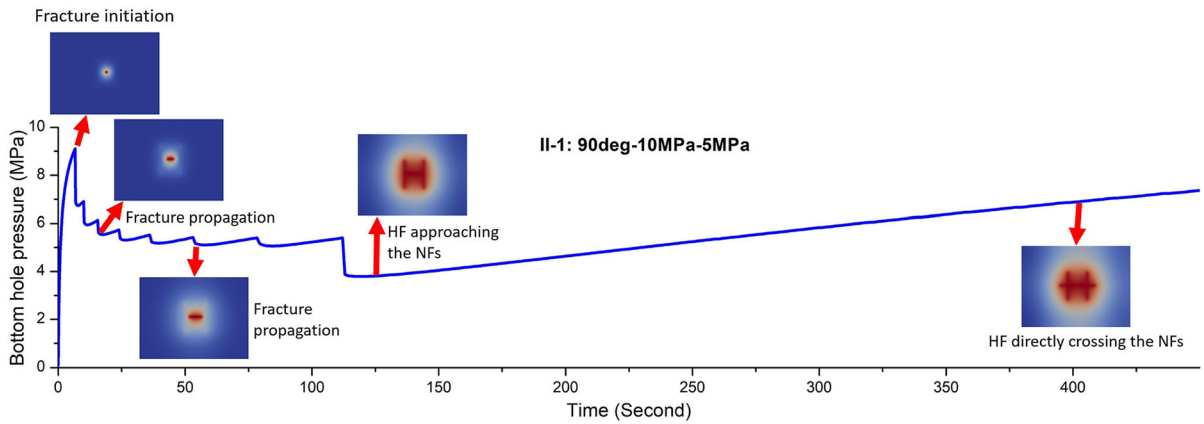
Fig. 11 The bottom hole pressure versus the injection time for the direct crossing case II-1. Approaching angle is 90 degrees. The maximum and minimum principal stresses are 10 MPa and 5 MPa, respectively
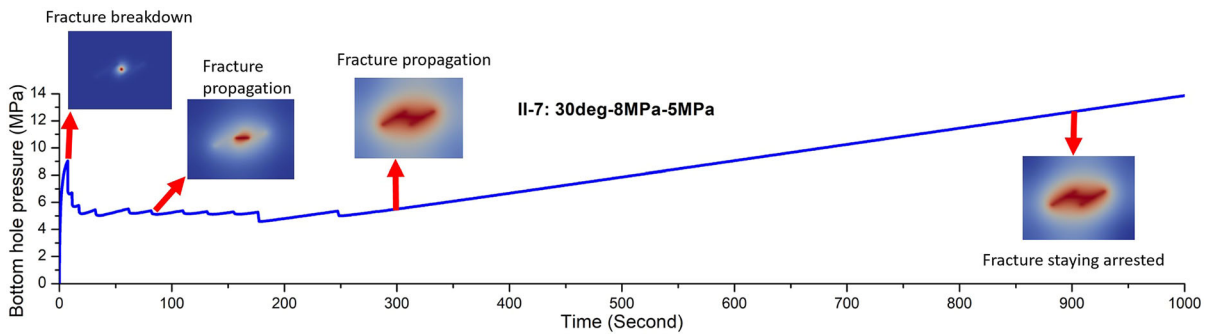
Fig. 12 The bottom hole pressure versus the injection time for the staying arrested case II-7. Approaching angle is 30 degrees. The maximum and minimum principal stresses are 8 MPa and 3 MPa, respectively

and low angles of approach (Cases I-1 and I-2) indicate a smaller stress difference enhances the potential for the hydraulic fracture arrest at the natural fracture, resulting in an increase in wellbore pressure due to the arrested propagation. Approach angle and differential stress have additive normal stress effects on the natural fractures. An increase in approach angle and stress difference tends to favor crossing; otherwise, the natural fractures tend to hinder direct crossing and arrest the hydraulic fracture with a concomitantly larger buildup in wellbore pressure. In addition, a comparison between low and intermediate friction for moderate approach angles (Cases I-3 and II-3) indicates that a higher coefficient of friction on the natural fracture promotes direct crossing. This results since it is less favorable to trigger slip or opening for natural fractures with a larger friction

coefficient. Thus, increasing shear strength enables the hydraulic fracture to directly transfer sufficient tensile stress to the opposite side of the natural fracture and induce tensile failure. A more detailed interpretation of influencing factors as to the behaviors of fracture propagation and interaction mechanisms will be presented in a subsequent paper (Table 5).

5 Scenario analysis

The hydraulic fracture initiates from the wellbore and propagates in the direction perpendicular to the minimum principal stress. When the hydraulic fracture approaches and intersects with natural fractures, various potential interaction scenarios result—viz. direct crossing, permanent arrest, and arrest with

Table 5 Mechanical properties used in the field simulation scenarios

Depth (m)	200	Hurst et al. (2011)
Gradient of vertical stress (MPa/m)	0.025	Han et al. (2016)
Ratio of mean horizontal stress to vertical stress at shallow depth	$300 \times$ depth $+ 1.14$	Han et al. (2016)
Injection rate typical of hydraulic fracturing in mudstone (kg/s)	4×10^{-4}	Wang et al. (2016)
Shear modulus of mudstone (GPa)	15	Rutqvist et al. (2013); Grippa et al. (2019)
Tensile strength gradient of mudstone (kPa/m)	37.5	Cripps and Taylor (1981)
Ratio of tensile strength of mudstone to fracture cohesion	2	Bureau (2014)
Poisson's ratio	0.25	Rutqvist et al. (2013); Grippa et al. (2019)
Matrix porosity	0.01	Rutqvist et al. (2013); Grippa et al. (2019)
Biot coefficient	0.88	Rutqvist et al. (2013); Grippa et al. (2019)
Normal stiffness of discontinuity (GPa/m)	1	Rutqvist et al. (2013); Grippa et al. (2019)
Shear stiffness of discontinuity (GPa/m)	50	Rutqvist et al. (2013); Grippa et al. (2019)
Friction angle (deg)	40	Rutqvist et al. (2013); Grippa et al. (2019)
Dilation angle (deg)	3	Rutqvist et al. (2013); Grippa et al. (2019)

reinitiation, with current computational hardware and software configurations. We explore these various scenarios through modeling in the following.

5.1 Direct crossing

These simulations are conducted under constant injection rate. Wellbore pressure builds until the hydraulic fracture initiates from the wellbore. The hydraulic fracture then propagates when the subcritical propagation criterion is met. As the tip of the hydraulic fracture approaches then intersects the natural fracture, the excess stresses field ahead of the hydraulic fracture is transferred onto the natural fracture, increasing the apertures and permeability around the intersection point and allowing the wellbore pressure to drop. Since the condition required for direct crossing is satisfied in this case, the hydraulic fracture directly crosses the natural fractures. Meanwhile, the fluid pressure is partly dissipated by the small incremental extension of the hydraulic fracture per propagation step. However, this dissipation is insufficient to fully counteract the magnitude of wellbore pressure increase resulting from injection at the well. Thus, the wellbore pressure net builds even following the intersection and will build until the fracture meets the solution domain boundary and establishes a new steady state.

5.2 Permanent arrest

As the fracture tip approaches the natural fracture, the bottom hole pressure reduces with incremental fracture propagation. The stress field ahead of the approaching hydraulic fracture tip increases the aperture of the natural fracture due to the tensile effects ahead of the approaching fracture tip, thereby increasing the conductive flow rate. After intersection of the HF with the natural fracture, the HF is expected to arrest at the natural fracture, at least momentarily, as the direct crossing condition is not met. The fluid injection rate remains higher than the rate of fluid entering the fractures under pressurization during this arrested state. Since the reinitiation criterion is not satisfied in this case when the reinitiation resistance is negative along the natural fracture following the quantitative analysis in Sect. 2.4, the parent hydraulic fracture remains arrested by the natural fracture.

5.3 Arrest with reinitiation

Following a similar procedure of fracture initiation, incremental propagation, and approach toward the natural fracture as for the previous arrested case (II-7), the hydraulic fracture again arrests momentarily after failing a direct crossing. During the temporary arrested state, the overall fracture pressure builds until the reinitiation criterion is satisfied at the most vulnerable location on the natural fracture, when the reinitiation
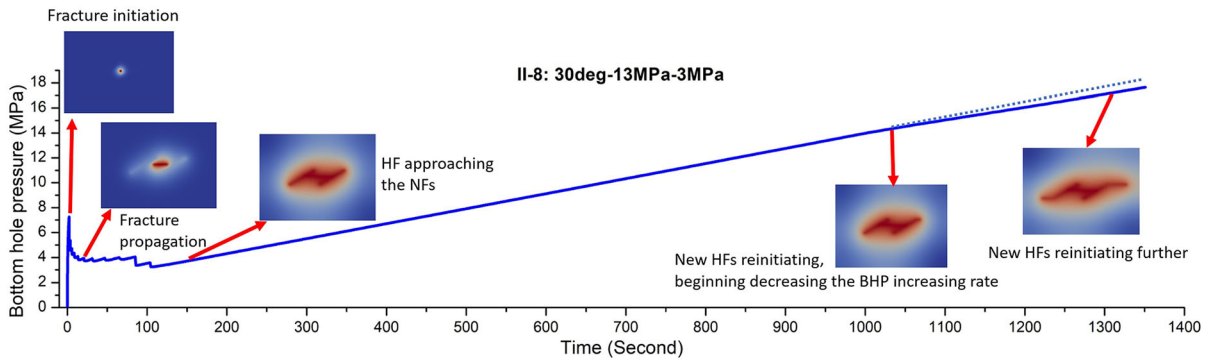
Fig. 13 The bottom hole pressure history versus the injection time for reinitiating case II-8. Approaching angle is 30 degrees. The maximum and minimum principal stresses are 13 MPa and 3 MPa, respectively

resistance is positive (Fig. 4) along the natural fracture and following the quantitative analysis of Sect. 2.4. The reinitiating fracture enhances the density of the fracture network through its intersection with other natural fractures, and facilitates fluid flow through the fractured reservoir. These reinitiated fractures in-turn propagate and reduce the rate of wellbore pressure buildup, shown as changing from the pre-reinitiation dashed blue line to the post-reinitiation solid blue line in Fig. 13.

5.4 Discussion of modelling of analogue of sand injectites

In general, regionally-developed sand injectites may locally harbour commercial volumes of hydrocarbons, act as fluid migration routes, and may provide high quality intra-reservoir flow units that create field-wide vertical communication through low permeability units. The various sandstone intrusions may also significantly modify the hydraulic fracture network.

As discontinuities can form fluid flow conduits in otherwise low permeability units, they facilitate fluid flow from sand intrusions, and may also increase the average vertical permeability to exceed the average horizontal permeability. In summary, the non-stratiform character of sand intrusions requires the use of hydraulic fracturing to facilitate effective hydrocarbon recovery from sand injectites (Hurst et al. 2007, 2017).

A model (Fig. 15) is constructed based on a realistic distribution if sand injectite dikes are representative of Panoche Hills (Fig. 14), in which the patterns and properties of natural discontinuities and matrix are represented as the analogues of Panoche sand injectites.

In quantitative modelling of this parametric study (Figs. 14 and 15), the magnitudes of the initial stress states are used that are representative of sand injectites during their formation. This sand injectite swarm is located at a depth of $\sim$ 200 m within a syncline with the geometry and distribution of the natural discontinuities recovered from Fig. 14. The gradient of

Fig. 14 Different angles of dikes (represented by black dashed lines) from the upper part of the intrusive complex (Hurst et al. 2011)
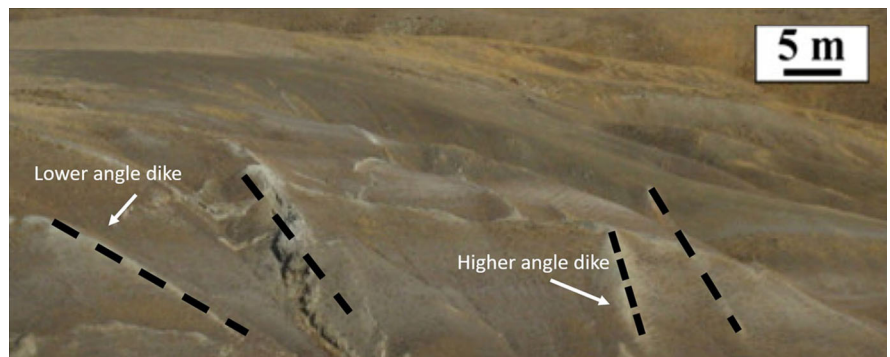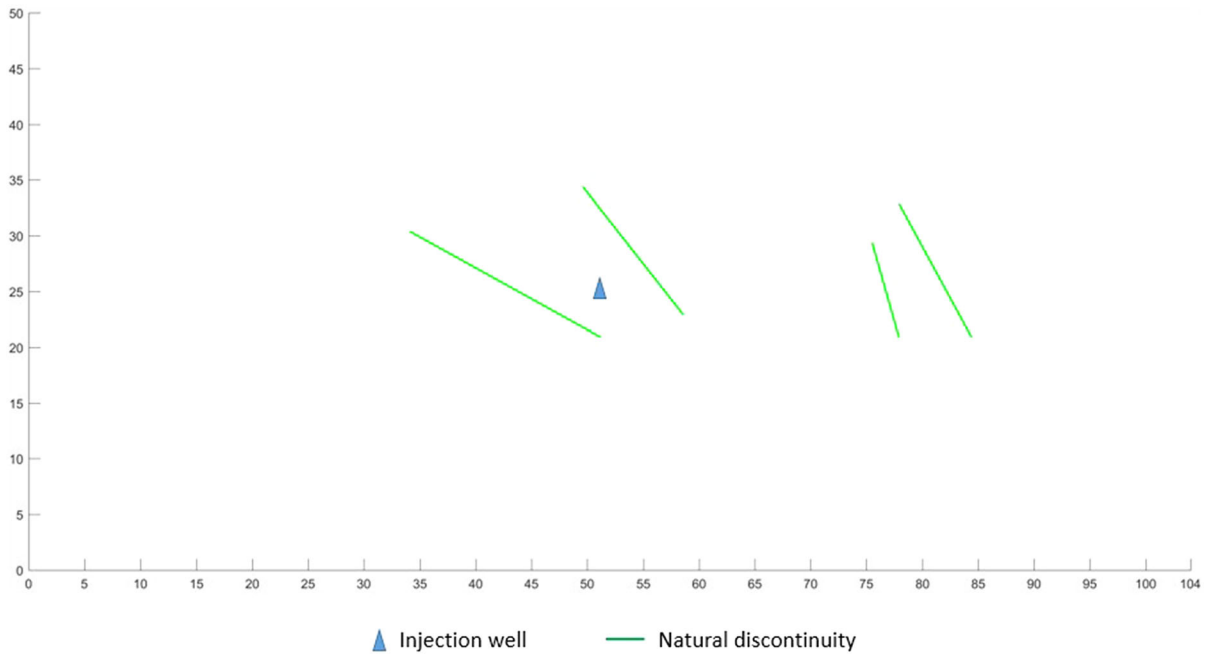
Fig. 15 The constructed conceptual model in which the patterns of natural discontinuities are represented as the analogue of a realistic sand injectites network
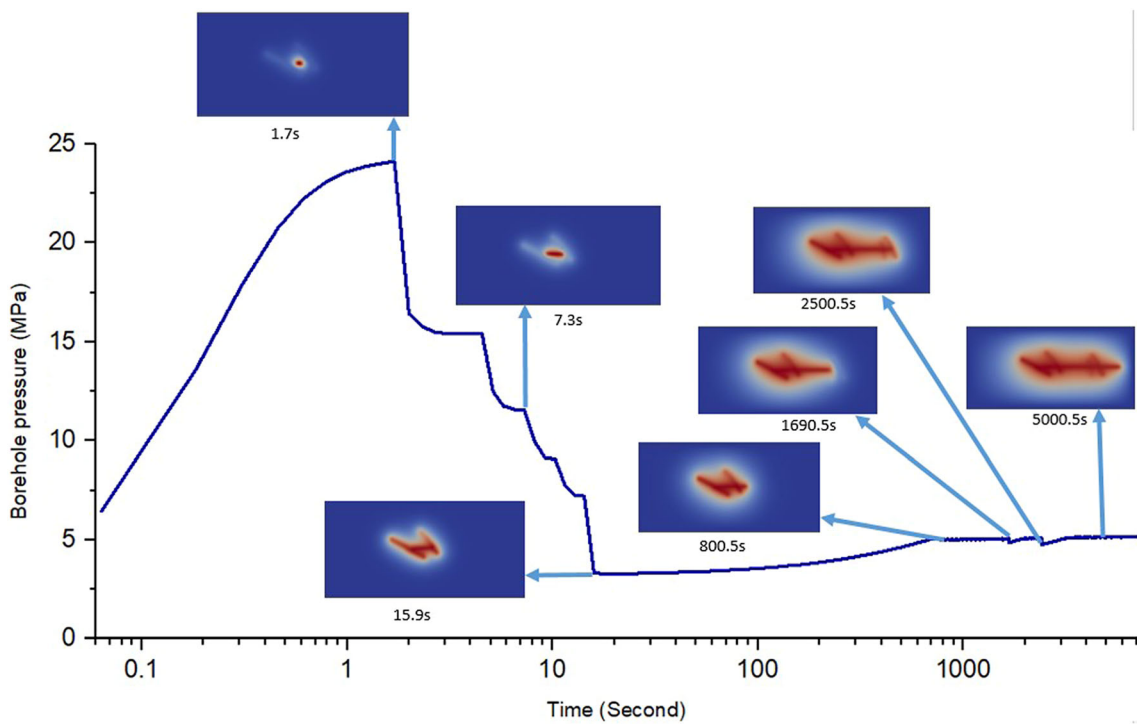

Fig. 16 The borehole pressure history curve, fracture patterns and pressure distributions at different times during the process of hydraulic fracture crossing the three natural discontinuities with higher approaching angles on the right side, while getting arrested by the left-most natural discontinuity with a lower approaching angle

vertical stress with depth is ~ 0.025 MPa/m. In this shallow synclinal environment, the ratio of the mean horizontal stress to vertical stress at shallow depth is of the order of $(300 \times \text{depth (meter)} + 1.14)$ (MPa) (Han et al. 2016). Mechanical properties and physical characteristics of the matrix and discontinuities used in the simulations are based on representative data for other sand injectites (Grippa et al. 2019). An injection wellbore is assumed embedded at the center of the model. A realistic and reasonable water injection rate (4×10^{-4} kg/s) suitable for successful industrial hydraulic fracturing in shales is applied (Wang et al. 2016). The fluid overpressure caused by the constantly injected fluid propagates a hydraulic fracture into the otherwise lower permeability matrix, until it intersects with the natural discontinuities and thus creates a more complex network of discontinuities. This potentially enhances the field scale permeability and facilitates fluid flow and hydrocarbon production from sand injectite features including dikes.

The simulation results for this analogue model (Fig. 16) demonstrate that the hydraulic fracture crosses the three natural discontinuities on the right side of the model where the approach angle is high but is arrested by the left-most natural discontinuity which it approaches at only a low angle. This is because the crossing criterion has been met for the three natural discontinuities to the right but not for the left-most one. The reinitiation criterion is also not met for the left-most natural discontinuities—the reinitiation resistance along the left natural discontinuity is not overcome by the fluid pressure within it.

The injection well is placed in the geometric center of the model—located between the leftmost two natural discontinuities. Apparent from Fig. 17a is that the permeability of the natural discontinuities is greatly enhanced by ~ 2 orders of magnitude (from 10^{-14} to 10^{-12} m^2) after the propagating hydraulic fracture approaches then interests with them. The increase in the permeability of the natural discontinuities results from their dilation (Fig. 17a) with differences in the initial magnitudes of apertures influenced by their different normal closures in their natural state. The propagating hydraulic fracture arrives near concurrently at the leftmost two natural discontinuities (~ 755 s) although arriving from different directions. The right wing of the propagating hydraulic fracture crosses the second-leftmost natural discontinuity, then

arrives at the third (~ 2090s) then fourth (~ 3395 s) fracture (Fig. 17).

The continuous propagation of the hydraulic fracture and fluid loss into the natural discontinuities deplete the wellbore pressure, resulting in a slight decline in fracture permeability following intersection (Fig. 17a)—concurrent with leakoff. The aperture (Fig. 17b) and corresponding permeability of the left-most natural discontinuity are highest immediately following intersection by the hydraulic fracture and in continuing its propagation (e.g., at ~ 4000 s). This is because the left endpoint of the hydraulic fracture is arrested by the left-most natural discontinuity and without extension hence depletes the otherwise pressure loss, thereby leading to a relatively higher permeability due to a relatively larger pressure increase and aperture enhancement than in the remainder of the three natural discontinuities crossed directly by the hydraulic fracture.

The results also demonstrate that the distribution of natural discontinuities controls fluid flow paths and pressure distribution, with significant permeability enhancement in the natural discontinuities, which could become intrusive traps as a result of hydraulic fracturing and evolution of networks to facilitate reservoir production. Also apparently the gross permeability of these otherwise low-permeability reservoirs at shallow depth can be greatly increased to facilitate fluid migration via hydraulic fracturing.

6 Conclusions

We present the development and verification of an integrated coupled thermo-hydro-mechanical-chemical (THMC) model, representing the HM process of hydraulic fracture propagation and interaction with natural fractures. The work is motivated by modelling of an analogue of Panoche sand injectite reservoirs with complex natural discontinuity networks. The assessment of fracture propagation and interaction is essential in predicting hydraulic fracturing connectivities with natural discontinuities and in defining flow paths for reservoir management in large-scale sand injectite systems.

Simulating fracture propagation using continuum approaches has the advantage of allowing long-term simulation in large scale reservoirs. Multiple constitutive models accommodating stress intensity factors,
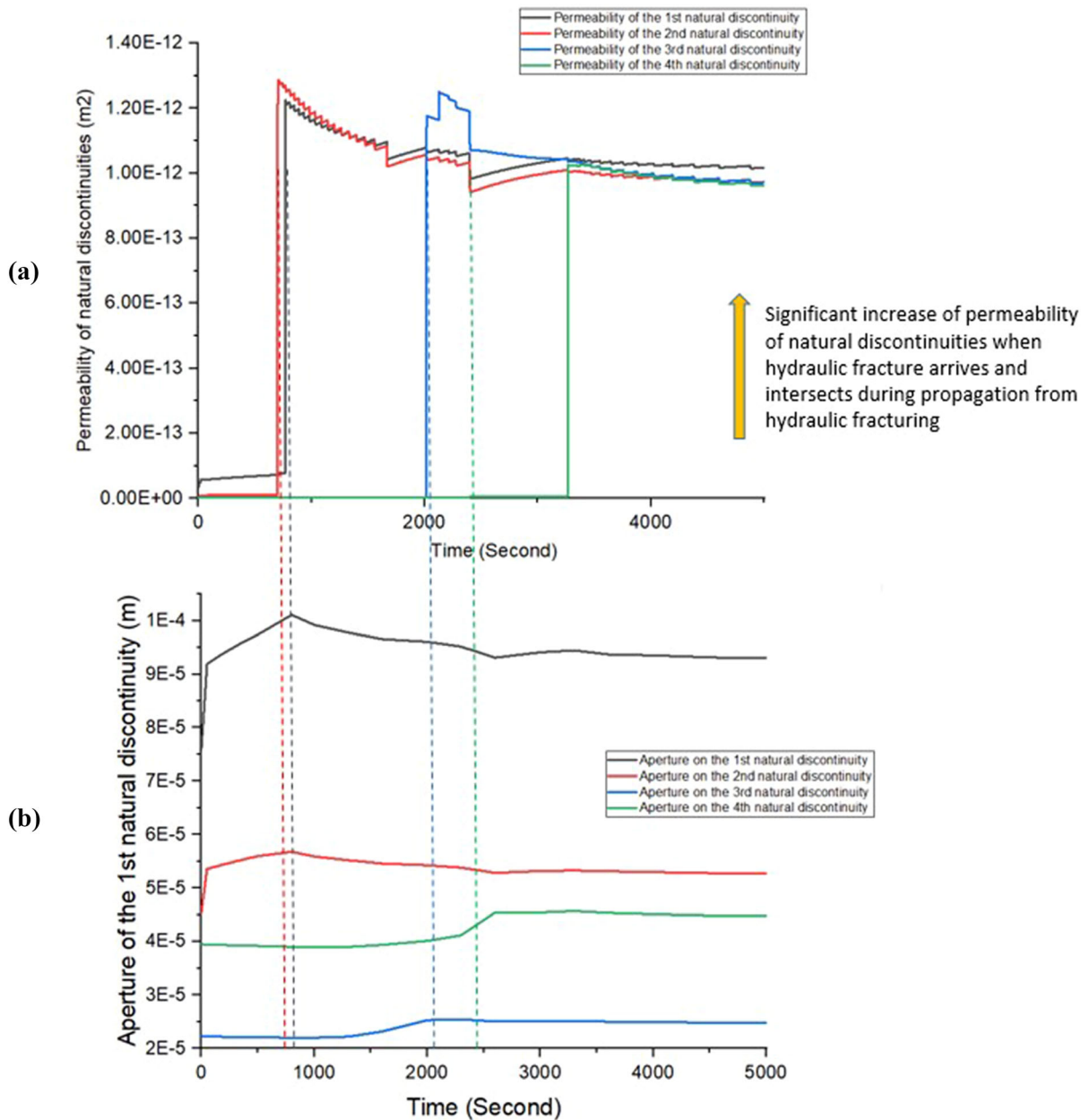
Fig. 17 Evolution of (**a**) permeability, and (**b**) aperture of natural discontinuities against time. The overall permeability of natural discontinuities increases greatly when the hydraulic fracture arrives and intersects with them with enhanced aperture

tip stress corrections, subcritical fracture propagation criteria, fracture advance lengths and fracture interaction mechanisms may all be characterized in order to accurately capture the response of fracture growth due to pressurization. The tip stress is corrected by quantifying the local stress state of the fracture tips

from the stress states of the neighboring elements. The fracture advance lengths are determined by using the stress intensity factors and the energy release rates during each propagation event. The potential interaction scenarios between the hydraulic and natural fractures are primarily governed by the stress state

exerted on the natural fractures and tensile strength of rock. Numerical results for predicting fracture propagation and interaction are verified against experimental observations, including those for hydraulic fractures directly crossing, remaining arrested, or reinitiating from natural fractures. The combined effects of approach angle and differential stress impact the magnitude of aperture by changing the normal closure response of the natural fractures. Higher approach angles and elevated deviatoric stresses generally favor direct crossing. Otherwise, the hydraulic fracture will be arrested by the natural fractures, or reinitiate from weak points on the natural fractures, as the approach angles and stress differences are both reduced. Also, it is easier to trigger direct crossing where the crossed fracture has a larger friction coefficient. This indicates that higher shear strength facilitates the direct crossing of natural fractures by transferring sufficient tensile stresses around the tip of the hydraulic fracture to the other side of the natural fracture. A comparison of results between simulations and experimental observations shows good agreement, confirming the applicability and usefulness of this numerical tool to simulate fracture propagation and interaction in fractured rock masses.

Finally, the analogue model of Panoche sand injectites accurately captures hydraulic fracture propagation in naturally fractured reservoirs and the development of geometrically-complex discontinuity networks,. These include choice of optimal locations and injection schedules to best connect the hydraulic and natural discontinuities under the influence of evolving stress and pressure and to support planning and drilling of field developments from these new unconventional intrusive traps, which are generally untested in many petroleum systems (Hurst and Vigorito 2017). The application to the modelling of Panoche sand injectites confirms that the field-scale permeability of sand injectites can be significantly increased by ~ 2 orders of magnitude after the hydraulic fracture connects the natural discontinuities which are sand injectites features to facilitate fluid flow in otherwise low-permeability matrix. The arrest of hydraulic fracture by the natural discontinuity leads to higher fracture pressure buildup which accentuates permeability enhancement than the direct crossing of the hydraulic fracture which dissipates more fluid pressure during propagation.

References

Anderson OL, Grew PC (1977) Stress corrosion theory of crack propagation with applications to geophysics. Rev Geophys Space Sci 15(1):77–104

Atkinson BK (1984) Subcritical crack-growth in geological-materials. J Geophys Res 89:4077–4114. https://doi.org/10.1029/JB089iB06p04077

Atkinson BK (1987) Fracture mechanics of rock. Academic Press, London

Atkinson C, Cook JM (1993) Effect of loading rate on crack propagation under compressive stress in a saturated porous material. J Geophys Res Solid Earth 98:6383–6395. https://doi.org/10.1029/92JB02413

Atkinson BK, Meredith PG (1987) The theory of subcritical crack growth with application to minerals and rocks. In: Atkinson BK (ed) Fracture mechanics of rock. Academic Press, London, pp 111–166

Atkinson BK, Meredith PG (1987) Experimental fracture mechanics data for rocks and minerals. In: Atkinson BK (ed) Fracture mechanics of rock. Academic Press, London, pp 477–525

Barenblatt GI (1962) The mathematical theory of equilibrium cracks in brittle fracture. Adv Appl Mech 7:55–129. https://doi.org/10.1016/S0065-2156(08)70121-2

Blanton TL (1982) An experimental study of interaction between hydraulically induced and pre-existing fractures. SPE/DOE unconventional gas recovery symposium of the society of petroleum engineers, Pittsburgh, PA, May 16–18, SPE/DOE 10847. https://doi.org/10.2118/10847-MS

Blanton TL (1986) Propagation of hydraulically and dynamically induced fractures in naturally fractured reservoirs. Unconventional gas technology symposium of the society of petroleum engineers, Louisville, KY, May 18–21. SPE 15261. https://doi.org/10.2118/15261-MS

Briedis NA, Bergslien D, Hjellbakk A, Hill RE, Moir GJ (2007) Recognition criteria, significance to field performance, and reservoir modeling of sand injections in the Balder field. North Sea AAPG Memoir 87:91–102. https://doi.org/10.1306/1209853M873259

Bureau D, Mourgues R, Cartwright J (2014) Use of a new artificial cohesive material for physical modelling: application to sandstone intrusions and associated fracture networks. J Struct Geol 66:223–236. https://doi.org/10.1016/j.jsg.2014.05.024

Cartwright JA, Huuse M, Aplin A (2007) Seal bypass systems. AAPG Bull 91:1141–1166. https://doi.org/10.1306/04090705181

Charles RJ (1958) Static fatigue of glass. I J Appl Phys 29:1549–1560. https://doi.org/10.1063/1.1722991

Chen Z, Bunger AP, Zhang X, Jeffrey RG (2009) Cohesive zone finite element-based modeling of hydraulic fractures. Acta Mech Solida Sin 22:443–452. https://doi.org/10.1016/S0894-9166(09)60295-0

Costin LS (1987) Time-dependent deformation and failure. In: Atkinson BK (ed) Fracture mechanics of rock. Academic Press, London, pp 167–215

Cripps JC, Taylor RK (1981) The engineering properties of mudrocks. Q J Eng Geol Hydrogeol 14:325–346. https://doi.org/10.1144/GSL.QJEG.1981.014.04.10

Crofton S (2014). Fundamentals of fracture mechanics. Imperial College London

Delaney PT, Pollard DD, Ziony JI, McKee EH (1986) Field relations between dikes and joints: emplacement processes and paleostress analysis. J Geophys Res Solid Earth 91:4920–4938. https://doi.org/10.1029/JB091iB05p04920

Dixon RJ, Schofield K, Anderton R, Reynolds AD, Alexander RWS, Williams MC, and Davies KG (1995) Sandstone diapirism and clastic intrusion in the Tertiary sub-marine fans of the Bruce-Beryl Embayment, Quadrant 9, UKCS. In: Hartley AJ, Prosser DJ (eds) Characterization of deep marine clastic systems, geological society, London, Special Publications, vol 94, pp 77–94. https://doi.org/10.1144/GSL.SP.1995.094.01.07

Dollar A, Steif PS (1989) A tension crack impinging upon frictional interfaces. ASME J Appl Mech 56(2):291–298. https://doi.org/10.1115/1.3176081

Dugdale DS (1960) Yielding of steel sheets containing slits. J Mech Phys Solids 8:100–108. https://doi.org/10.1016/0022-5096(60)90013-2

Dyer JR (1983) Jointing in sandstones, Arches National Park, Utah. Dissertation, Stanford University

Evans AG, Blumenthal W (1983) High temperature failure in ceramics. In: Bradt RC, Evans AG, Hasselman DPH, Lange FF (eds) Fracture mechanics of ceramics. Volume 6: measurements, transformations, and high-temperature fracture. Plenum Press, New York, pp 423–448

Evans AG, Charles EA (1976) Fracture toughness determinations by indentation. J Am Ceram Soc 59(7–8):371–372. https://doi.org/10.1111/j.1151-2916.1976.tb10991.x

Gan Q, Elsworth D (2016) A continuum model for coupled stress and fluid flow in discrete fracture networks. Geomech Geophys Geo-energ Geo-resour 2:43–61. https://doi.org/10.1007/s40948-015-0020-0

Gan Q, Elsworth D, Zhao Y, Grippa A, Hurst A (2020) Coupled hydro-mehaical evolution of fracture permeability in sand injectite intrusions. J Rock Mech Geotech Eng 12:742–751. https://doi.org/10.1016/j.jrmge.2019.10.007

Gdoutos EE (2003) Calculation of stress intensity factors by the Westergaard method. In: Gdoutos EE, Rodopoulos CA, Yates JR (eds) Problems of fracture mechanics and fatigue. Springer, Dordrecht. https://doi.org/10.1007/978-94-017-2774-7_5

Ghamgosar M, Erarslan N (2016) Experimental and numerical studies on development of fracture process zone (FPZ) in rocks under cyclic and static loadings. Rock Mech Rock Eng 49(3):893–908. https://doi.org/10.1007/s00603-015-0793-z

Griffith AA (1921) The phenomena of rupture and flow in solids. Philos Trans A Math Phys Eng Sci 221(582–593):163–198. https://doi.org/10.1098/rsta.1921.0006

Grippa A, Hurst A, Palladino G, Lacopini D, Lecomte I, Huuse M (2019) Seismic imaging of complex geometry: forward modeling of sandstone intrusions. Earth Planet Sc Lett 513:51–63. https://doi.org/10.1016/j.epsl.2019.02.011

Gu H, Weng X (2010) Criterion for fractures crossing frictional interfaces at non-orthogonal angles. American Rock Mechanics Association

Gurney C, Hunt J (1967) Quasi-static crack propagation. Proc R Soc Lond A 299:508–524. https://doi.org/10.1098/rspa.1967.0152

Han J, Zhang H, Liang B, Rong H, Lan T, Liu Y, and Ren T (2016) Influence of large syncline on in situ stress field: a case study of the Kaiping Coalfield, China. Rock Mech Rock Eng. https://doi.org/10.1007/s00603-016-1039-4

Hillerborg A, Modeer M, Petersson P (1976) Analysis of crack formation and crack growth in concrete by means of fracture mechanics and finite elements. Cem Concr Res 6(6):773–782. https://doi.org/10.1016/0008-8846(76)90007-7

Hubbert MK, Willis DG (1957) Mechanics of hydraulic fracturing. Soc Pet Eng AIME J 210:153–163. https://doi.org/10.2118/686-G

Hurst A, Vigorito M (2017) Saucer-shaped sandstone intrusions: an underplayed reservoir target. AAPG Bull 101(4):625–633. https://doi.org/10.1306/011817DIG17070

Hurst A, Cartwright JA, Duranti D (2003) Fluidization structures produced by upward injection of sand through a sealing lithology. Geol Soc Spec Publ 216:123–137. https://doi.org/10.1144/GSL.SP.2003.216.01.09

Hurst A, Huuse M, Cartwright JA, Duranti D (2007) Sand injectites in deep-water clastic reservoirs: are they there and do they matter? AAPG Stud Geol 56:24. https://doi.org/10.1306/12401014St561546

Hurst A, Scott A, Vigorito M (2011) Physical characteristics of sand injectites. Earth Sci Rev 106:215–246. https://doi.org/10.1016/j.earscirev.2011.02.004

Hurst A and Cartwright JA (2007) Relevance of sand injectites to hydrocarbon exploration and production. In: Hurst A, Cartwright J (eds) Sand injectites: implications for hydrocarbon exploration and production. AAPG Memoir 87, Tulsa, pp 1–19. https://doi.org/10.1306/1209846M871546

Hurst A, Cartwright JA, Duranti D, Huuse M, and Nelson M (2005) Sand injectites: an emerging global play in deep-water clastic environments In: Dore A, Vining B (eds) Petroleum geology: north-west Europe and global perspectives—proceedings of the 6th petroleum geology conference. Geology Society, London, pp 133–144. https://doi.org/10.1144/0060133

Huuse M, Cartwright JA, Gras R, Hurst A (2005) Kilometer-scale sandstone intrusions in the Eocene of the Outer Moray Firth (UK North Sea): migration paths, reservoirs and potential drilling hazards. In: Proceedings of the 6th petroleum geology conference. London, pp 1577–1594. https://doi.org/10.1144/0061577

Irwin GR (1948) Fracture dynamics. In: Fracturing of metals. Amer. Soc. For Metals, pp 147–166

Irwin GR (1956) Onset of fast crack propagation in high strength steels and aluminium alloys, NRL Report 4763

Irwin GR (1958) Fracture. In: Flügge S (ed) Handbuch der Physik. V. VI elasticity and plasticity Berlin. Springer, pp 551–590

Irwin GR (1960) Plastic zone near a crack and fracture toughness. In: Proceedings of the 7th Sagamore ordnance materials conference. New York

Itasca Consulting Group, Inc (2000) FLAC3D. Fast Lagrangian analysis of continua in three-dimensions, ver. 5.0. Itasca, Minneapolis

Jaeger JC, Cook NGW, Zimmerman RW (2007) Fundamental of rock mechanics. Blackwell Publishers

Jaeger JC (1979) Fundamentals of rock mechanics, 3rd edn. Chapman Hall, New York.

Kachanov LM (1958) IZV. Akad. Nauk. USSR. OTN (No. 8)

Karunaratne BSB, Lewis MH (1980) High-temperature fracture and diffusional deformation mechanisms in Si-Al-O-N ceramics. J Mater Sci 15:449–462. https://doi.org/10.1007/BF00551698

Lawn B, Wilshaw R (1975) Indentation fracture: principles and applications. J Mater Sci 10:1049–1081

Lawn B (1993) Fracture of brittle solids, 2nd edn. Cambridge Solid State Science Series

Li M, Tang S, Guo T, Qi M (2018) Numerical investigation of hydraulic fracture propagation in the glutenite reservoir. J Geophys Eng 15:2124–2138. https://doi.org/10.1088/1742-2140/aaba27

Liu Z, Chen M, Zhang G (2014) Analysis of the influence of a natural fracture network on hydraulic fracture propagation in carbonate formations. Rock Mech Rock Eng 47(2):575–587. https://doi.org/10.1007/s00603-013-0414-7

Mergheim J, Kuhl E, Steinmann P (2005) A finite element method for the computational modeling of cohesive cracks. Int J Numer Meth Eng 63(2):276–289. https://doi.org/10.1002/nme.1286

Neuber H (1937) Kerbspannungslehre. Springer, Berlin

Oda M (1986) An equivalent continuum model for coupled stress and fluid flow analysis in jointed rock masses. Water Resour Res 22:1845–1856. https://doi.org/10.1029/WR022i013p01845

Odling N (1997) Scaling and connectivity of joint systems in sandstones from western Norway. J Struct Geol 19:1257–1271. https://doi.org/10.1016/S0191-8141(97)00041-2

Olson JE (1993) Joint pattern development: effects of subcritical crack-growth and mechanical crack interaction. J Geophys Res 98:12251–12265. https://doi.org/10.1029/93JB00779

Olson JE (2003) Sublinear scaling of fracture aperture versus length: an exception or the rule? J Geophys Res 108(B9):2413. https://doi.org/10.1029/2001JB000419

Olson JE, Holder J and Rijken P (2002) Quantifying the fracture mechanics properties of rock for fractured reservoir. In: Proceedings of the SPE/ISRM rock mechanics in petroleum engineering conference. SPE, Richardson, TX, pp 421–432. https://doi.org/10.2118/78207-MS

Orowan E (1949) Fracture and strength of solids. Rep Prog XII 185–232. https://doi.org/10.1088/0034-4885/12/1/309

Paluszny A, Matthai S (2009) Numerical modeling of discrete multi-crack growth applied to pattern formation in geological brittle media. Int J Solids Struct 46:3383–3397. https://doi.org/10.1016/j.ijsolstr.2009.05.007

Paris PC, Erdogan F (1963) A critical analysis of crack propagation laws. Trans ASME J Basic Eng 85(1):528–534. https://doi.org/10.1115/1.3656900

Pollard DD (1987) Elementary fractures mechanics applied to the structural interpretation of dykes. In: Halls HC, Fahrig WH (eds) Mafic dyke swarms, Vol. 34, Geological Association of Canada, Canada, pp 112–128. Geological Association of Canada Special Paper

Ren X, Zhou L, Li H, Lu Y (2019) A three-dimensional numerical investigation of the propagation path of a two-cluster fracture system in horizontal wells. J Pet Sci Eng 173:1222–1235. https://doi.org/10.1016/j.petrol.2018.10.105

Renshaw CE, Pollard DD (1994) Numerical simulation of fracture set formation: a fracture mechanics model consistent with experimental observations. J Geophys Res 99:9359–9372. https://doi.org/10.1029/94JB00139

Renshaw CE, Pollard DD (1995) An experimentally verified criterion for propagation across unbounded frictional interfaces in brittle, linear elastic materials. Int J Rock Mech Min Sci Geomech Abstr 32:237–249. https://doi.org/10.1016/0148-9062(94)00037-4

Rutqvist J, Leung C, Hoch A, Wang Y, Wang Z (2013) Linked multicontinuum and crack tensor approach for modeling of coupled geomechanics, fluid flow and transport in fractured rock. J Rock Mech Geotech Eng 5:18–31. https://doi.org/10.1016/j.jrmge.2012.08.001

Sarmadivaleh M, Rasouli V (2014) Modified Reinshaw and Pollard criteria for a non-orthogonal cohesive natural interface intersected by an induced fracture. Rock Mech Rock Eng 47:2107–2115. https://doi.org/10.1007/s00603-013-0509-1

Schmidt RA, Lutz TJ (1979) KIc and JIc of Westerly granite—effects of thickness and in-plane dimensions. Fract Mech Appl Brittle Mater ASTM STP 678:166–182. https://doi.org/10.1520/STP36635S

Scott A, Hurst A, Vigorito M (2013) Outcrop-based reservoir characterization of a kilometer-scale sand-injectite complex. AAPG Bull 97:309–343. https://doi.org/10.1306/05141211184

Segall P (1984a) Rate-dependent extensional deformation resulting from crack growth in rock. J Geophys Res 89–B6:4185–4195. https://doi.org/10.1029/JB089iB06p04185

Segall P (1984b) Formation and growth of extensional fracture sets. Geol Soc Am Bull 95:454–462. https://doi.org/10.1130/0016-7606(1984)95%3c454:FAGOEF%3e2.0.CO;2

Selvadurai APS, Zhang D, Kang Y (2018) Permeability evolution in natural fractures and their potential influence on loss of productivity in ultra-deep gas reservoirs of the Tarim Basin, China. J Nat Gas Sci Eng 58:162–177. https://doi.org/10.1016/j.jngse.2018.07.026

Senseny PE, Pfeifle TW (1984) Fracture toughness of sandstones and shales. In Presented at the 25th U.S. symposium on rock mechanics. Evanston, Illinois

Sun CT, Jin ZH (2012) Fracture mechanics. Elsevier

Taleghani AD (2009) Analysis of hydraulic fracture propagation in fractured reservoirs: an improved model for the interaction between induced and natural fractures. Dissertation, The University of Texas at Austin

Taron J, Elsworth D (2009) Thermal-hydrologic-mechanical-chemical processes in the evolution of engineered geothermal reservoirs. Int J Rock Mech Min Sci 46:855–864. https://doi.org/10.1016/j.ijrmms.2009.01.007

Taylor BJ (1982) Sedimentary dikes, pipes and related structures in the Mesozoic sediments of southeastern Alexander Island. Antarct Sci 51:1–42

Valko P, Economides MJ (1994) Propagation of hydraulically induced fractures—a continuum damage mechanics approach. Int J Rock Mech Min Sci Geomech Abstr 31:221–229. https://doi.org/10.1016/0148-9062(94)90466-9

Valko P, Economides MJ (1995) Hydraulic fracture mechanics. Wiley, New York

Vigorito M, Hurst A (2010) Regional sand injectite architecture as a record of pore-pressure evolution and sand redistribution in the shallow crust: insights from the Panoche Giant Injection Complex, California. J Geol Soc 167(5):889–904. https://doi.org/10.1144/0016-76492010-004

Wan T, Yu Y, Sheng JJ (2015) Experimental and numerical study of the EOR potential in liquid-rich shales by cyclic gas injection. J Unconv Oil Gas Resour 12:56–67. https://doi.org/10.1016/j.juogr.2015.08.004

Wang Y, Li X, Tang CA (2016) Effect of injection rate on hydraulic fracturing in naturally fractured shale formations: a numerical study. Environ Earth Sci 75:935. https://doi.org/10.1007/s12665-016-5308-z

Warpinski NR, Teufel LW (1987) Influence of geologic discontinuities on hydraulic fracture propagation. J Pet Technol 39(02):209–220. https://doi.org/10.2118/13224-PA

Wells G (2001) Discontinuous modelling of strain localization and failure. Dissertation, Delft University of Technology

Xu T, Spycher N, Sonnenthal E, Zheng L, Pruess K (2012) TOUGHREACT user's guide: a simulation program for non-isothermal multiphase reactive transport in variable saturated geologic media, version 2.0. Technical report LBNL-DRAFT. Lawrence Berkeley National Laboratory (LBNL), University of California, Berkeley, California, USA

Zhang X, Jeffery RG (2006) The role of friction and secondary flaws on deflection and re-initiation of hydraulic fractures at orthogonal pre-existing fractures. Geop J Int 166(3):1454–1465. https://doi.org/10.1111/j.1365-246X.2006.03062.x

Zhou J, Chen M, Jin Y, Zhang G (2008) Analysis of fracture propagation behavior and fracture geometry using a tri-axial fracturing system in naturally fractured reservoirs. Int J Rock Mech Min Sci Geomech 45:1143–1152. https://doi.org/10.1016/j.ijrmms.2008.01.001

Zhou J, Zhang L, Pan Z, Han Z (2017) Numerical studies of interactions between hydraulic and natural fractures by Smooth Joint Model. J Nat Gas Sci Eng 46:592–602. https://doi.org/10.1016/j.jngse.2017.07.030

Zhou J, Zhang L, Braun A, Han Z (2017) Investigation of processes of interaction between hydraulic and natural fractures by PFC modeling comparing against laboratory experiments and analytical models. Energies 10(7):1001. https://doi.org/10.3390/en10071001

Zi G, Song JH, Budyn E, Lee SH, Belytschko T (2004) A method for growing multiple cracks without remeshing and its application to fatigue crack growth. Modell Simul Mater Sci Eng 12:901–915. https://doi.org/10.1088/0965-0393/12/5/009